

High-order superlattices by rolling up van der Waals heterostructures

<https://doi.org/10.1038/s41586-021-03338-0>

Received: 21 February 2020

Accepted: 8 February 2021

Published online: 17 March 2021

 Check for updates

Bei Zhao^{1,14}, Zhong Wan^{2,14}, Yuan Liu^{1,3}, Junqing Xu⁴, Xiangdong Yang¹, Dingyi Shen¹, Zucheng Zhang¹, Chunhao Guo⁴, Qi Qian^{2,5}, Jia Li¹, Ruixia Wu¹, Zhaoyang Lin², Xingxu Yan⁶, Bailing Li¹, Zhengwei Zhang¹, Hufang Ma¹, Bo Li¹, Xiao Chen⁷, Yi Qiao⁸, Imran Shakir⁹, Zeyad Almutairi^{9,10}, Fei Wei⁷, Yue Zhang^{8,11}, Xiaoqing Pan^{6,12}, Yu Huang^{5,13}, Yuan Ping⁴, Xidong Duan¹ & Xiangfeng Duan^{2,13}

Two-dimensional (2D) materials^{1,2} and the associated van der Waals (vdW) heterostructures^{3–7} have provided great flexibility for integrating distinct atomic layers beyond the traditional limits of lattice-matching requirements, through layer-by-layer mechanical restacking or sequential synthesis. However, the 2D vdW heterostructures explored so far have been usually limited to relatively simple heterostructures with a small number of blocks^{8–18}. The preparation of high-order vdW superlattices with larger number of alternating units is exponentially more difficult, owing to the limited yield and material damage associated with each sequential restacking or synthesis step^{8–29}. Here we report a straightforward approach to realizing high-order vdW superlattices by rolling up vdW heterostructures. We show that a capillary-force-driven rolling-up process can be used to delaminate synthetic SnS₂/WSe₂ vdW heterostructures from the growth substrate and produce SnS₂/WSe₂ roll-ups with alternating monolayers of WSe₂ and SnS₂, thus forming high-order SnS₂/WSe₂ vdW superlattices. The formation of these superlattices modulates the electronic band structure and the dimensionality, resulting in a transition of the transport characteristics from semiconducting to metallic, from 2D to one-dimensional (1D), with an angle-dependent linear magnetoresistance. This strategy can be extended to create diverse 2D/2D vdW superlattices, more complex 2D/2D/2D vdW superlattices, and beyond-2D materials, including three-dimensional (3D) thin-film materials and 1D nanowires, to generate mixed-dimensional vdW superlattices, such as 3D/2D, 3D/2D/2D, 1D/2D and 1D/3D/2D vdW superlattices. This study demonstrates a general approach to producing high-order vdW superlattices with widely variable material compositions, dimensions, chirality and topology, and defines a rich material platform for both fundamental studies and technological applications.

The emergence of the atomically thin 2D layered materials has opened new avenues for exploring low-dimensional physics at the limit of single or few atomic layers, and for creating functional devices with unprecedented performance or unique functionalities^{1,2}. Beyond isolated 2D atomic layers, the mixing and matching of distinct 2D materials, such as graphene, hexagonal boron nitride and transition metal dichalcogenides, has enabled vast flexibility for creating 2D vdW heterostructures and vdW superlattices beyond the limits of lattice-matching requirements^{3–7}. These heterostructures and superlattices introduce a paradigm for engineering artificial materials with designable structural and electronic properties and enabling functions beyond the reach of existing materials^{8–18}.

So far, 2D vdW heterostructures and vdW superlattices have been mostly obtained through a mechanical exfoliation and arduous

layer-by-layer restacking process. This approach is generally applied to create diverse heterostructures from a wide range of layered crystals, but typically with limited yield and reproducibility, and becomes exponentially more challenging for high-order superlattices. Alternatively, chemical vapour deposition (CVD) approaches have also been explored for directly synthesizing 2D vdW heterostructures, but these are also usually limited to low-order structures with only two or few distinct blocks^{19–29}. The use of sequential vdW epitaxial growth to produce high-order vdW superlattices requires repeated switching between different chemical and thermal environments, which usually leads to serious structural degradation of the atomically thin crystals. Although this challenge may be partly mitigated through careful synthetic design to enable successful growth of 2D lateral superlattices^{30–32}, the growth of high-order 2D vdW superlattices using a similar strategy

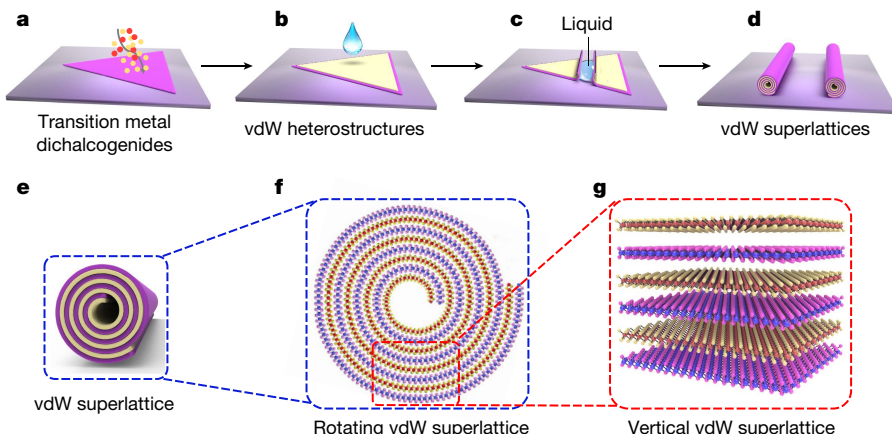


Fig. 1 | Schematic illustration of the fabrication process of roll-up vdW superlattices. **a**, vdW epitaxial growth of a second 2D material on top of a previously grown 2D material to form a vertically stacked heterobilayer vdW heterostructure. **b**, A drop of ethanol–water–ammonia solution is added onto the surface of the vdW heterostructure. **c**, The intercalation of liquid between the heterobilayer vdW heterostructure and the substrate delaminates the vdW heterostructure from the substrate, and the capillary force drives the spontaneous rolling-up process. **d**, Formation of vdW heterostructure roll-ups. **e**, Magnified schematic view of the roll-up. **f**, **g**, Further enlarged cross-sectional view of the vdW heterostructure roll-up. **g**, Schematic view of the high-order vdW superlattice in the vdW heterostructure roll-up.

is more challenging and has not been achieved yet. Additionally, an electrochemical molecular intercalation approach has been recently reported for creating high-order superlattices³³, but it is limited to only selected molecular systems. Despite considerable efforts and the successful construction of diverse vdW heterostructures, the fabrication of high-order stable vdW superlattices remains a challenge.

Herein we report a straightforward approach to create high-order vdW superlattices by rolling up 2D vdW heterostructures. By exposing CVD-grown 2D/2D vdW heterostructures (for example, SnS₂/WSe₂) to an ethanol–water–ammonia solution, we show that the capillary force can drive a spontaneous delamination and rolling-up process to produce vdW heterostructure roll-ups containing high-order 2D/2D vdW superlattices, without going through multiple transfer and restacking processes. Scanning transmission electron microscopy (STEM) and energy-dispersive X-ray spectroscopy (EDS) elemental mapping studies demonstrate highly periodic modulation of the atomic composition in the resulting vdW superlattices with an atomically sharp interface. Electrical transport studies reveal an evolution of the transport characteristics from 2D to 1D with greatly increased conductance, as well as an angle-dependent linear magnetoresistance, in the vdW superlattices. Furthermore, we show that this rolling-up strategy can be extended to create diverse 2D/2D vdW superlattices and complex three-component 2D/2D/2D vdW superlattices (SnS₂/MoS₂/WS₂), as well as beyond-2D materials, including 3D or 1D materials, generating a wide range of multi-dimensional vdW superlattices, such as 3D/2D (Al₂O₃/WSe₂), 3D/2D/2D (Al₂O₃/SnS₂/WSe₂), 1D/2D (Ag nanowire/WSe₂) and 1D/3D/2D (Ag nanowire/Al₂O₃/WSe₂) vdW superlattices.

The fabrication process of the roll-up vdW superlattices is schematically illustrated in Fig. 1. First, a 2D atomic crystal (for example, monolayer WSe₂) is grown on a SiO₂/Si substrate using a modified CVD process³⁴. Next, the resulting 2D crystals are used as templates for the vdW epitaxial growth of a second 2D material (such as SnS₂, SnSe₂, In₂Se₃ and Cr₃Te₈) to achieve the vdW heterostructures. To initiate the capillary-force-driven rolling-up process, an ethanol–water–ammonia solution is dropped onto the substrate-supported vdW heterostructures. There, the solution readily intercalates into the interface between the SnS₂/WSe₂ vdW heterostructures and the underlying SiO₂/Si substrate to delaminate the SnS₂/WSe₂ vdW heterostructures from the substrate and induce the spontaneous rolling-up process with the help of surface tension^{35,36}. Thus, 2D vdW heterostructure roll-ups containing high-order 2D vdW superlattices are produced (see Methods for details). Finally, focused-ion-beam milling is used to produce a cross-sectional slice of the roll-ups, which are analysed using high-resolution STEM and EDS elemental mapping studies.

We used SnS₂/WSe₂ vdW heterostructures as an initial example to demonstrate the rolling-up process to high-order vdW superlattices. Figure 2a, b shows optical microscopy images of a triangular

single-crystal domain of monolayer WSe₂ after the first-step CVD growth process, and a SnS₂/WSe₂ vdW heterobilayer after the second-step growth. Our studies indicate that SnS₂ preferentially nucleates on the WSe₂ template (rather than the SiO₂ substrate) and expands on WSe₂ through a vdW epitaxial growth process to form the 2D vdW heterostructures (Extended Data Fig. 1). The uniform optical contrast of the SnS₂/WSe₂ vertical heterobilayer (Fig. 2b) suggests that the WSe₂ monolayer is completely covered by the SnS₂ monolayer, forming the material foundation for the preparation of the roll-up vdW superlattices. Upon exposure to the ethanol–water–ammonia solution, the SnS₂/WSe₂ vdW heterostructures spontaneously roll up to form the SnS₂/WSe₂ roll-ups, as clearly shown in the corresponding optical microscopy image (Fig. 2c) and a representative scanning electron microscopy (SEM) image (Fig. 2d).

A representative cross-sectional STEM image further shows the roll-up structure (Fig. 2e), with the SnS₂ and WSe₂ layers in the SnS₂/WSe₂ vdW heterostructures winding around each other layer by layer to form a high-order vdW superlattice. The STEM image also shows areas in which the layers are not in intimate contact; these could be attributed to occasional particulate contamination trapped during the rolling-up process in a typical laboratory environment, or to strain generated during the cross-sectional STEM sample-preparation process. The higher-resolution STEM image reveals the atomically resolved SnS₂/WSe₂ vdW superlattice structure, which consists of alternating layers of monolayer WSe₂ and monolayer SnS₂ (Fig. 2f), as confirmed by EDS elemental mapping images (Fig. 2g–h). Additionally, the EDS intensity profiles clearly show alternating peaks for W and Sn, confirming the formation of SnS₂/WSe₂ vdW superlattices (Fig. 2i). Both the high-resolution STEM image (Fig. 2f) and the EDS line profiles (Fig. 2j) reveal a periodicity of 1.26 nm, which is consistent with the expected thickness of the repeating unit of the monolayer SnS₂/monolayer WSe₂ vdW heterostructure. The corresponding interlayer spacing between W atoms (Fig. 2j) and Sn atoms (Fig. 2k) in the higher-resolution STEM image (Fig. 2f) show a rather narrow distribution around 1.26 nm with a standard deviation of 0.01 nm, indicating the formation of highly uniform vdW superlattice. The distance between the monolayer SnS₂ and the monolayer WSe₂ in the vdW superlattice is 0.63 nm (Fig. 2l), which is essentially the same as the intrinsic interlayer distance, indicating a high-quality vdW interface with little interlayer contamination in the vdW superlattices. Together, these structure analyses clearly demonstrate that we have successfully produced high-quality, high-order 2D vdW superlattices with a high level of spatial uniformity.

The rolling-up process opens a straightforward path to high-order superlattices, allowing us to tailor the interlayer coupling, the dimensionality and the topology of the resulting superlattice structure. For example, the transformation of the SnS₂/WSe₂ bilayer vdW heterostructure into a high-order vdW superlattice could fundamentally modify its

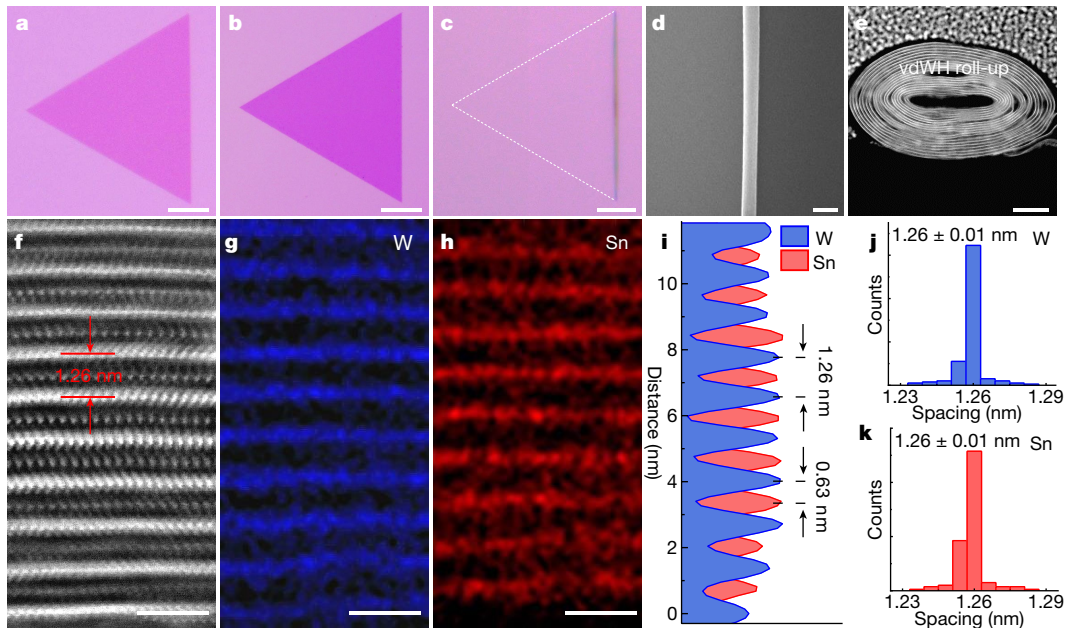


Fig. 2 | Structural characterizations of $\text{SnS}_2/\text{WSe}_2$ roll-ups and high-order vdW superlattices. **a–c**, Optical microscopy images of a WSe_2 monolayer (**a**), a $\text{SnS}_2/\text{WSe}_2$ heterobilayer vdW heterostructure (**b**) and a $\text{SnS}_2/\text{WSe}_2$ roll-up (**c**). Scale bars, 10 μm . **d**, SEM image of a representative $\text{SnS}_2/\text{WSe}_2$ roll-up. Scale bar, 200 nm. **e**, Cross-sectional STEM image of a representative $\text{SnS}_2/\text{WSe}_2$ roll-up. Scale bar, 20 nm. **f**, Higher-resolution cross-sectional STEM image of

the $\text{SnS}_2/\text{WSe}_2$ vdW superlattice. The bright and dark regions correspond to the WSe_2 and SnS_2 monolayers, respectively. Scale bar, 2 nm. **g, h**, Corresponding EDS mapping images for W (**g**) and Sn (**h**). Scale bars, 2 nm. **i**, EDS intensity profiles for W (blue) and Sn (red). **j, k**, Statistical distribution of interlayer spacing between W atoms (**j**) and Sn atoms (**k**).

band structure and thus its electronic properties. To explore such an effect, we conducted first-principle calculations based on many-body perturbation theory (GW approximation)³⁷ to probe the electronic band structure of the resulting vdW superlattices. The unit cell for the calculation was based on a $10 \times 10 \text{ WSe}_2/9 \times 9 \text{ SnS}_2$ supercell consistent with the lattice constants of both WSe_2 and SnS_2 (Extended Data Fig. 2a). We note that a direct GW approximation for such a large interface is computationally formidable; therefore, we implemented an efficient screening approach to account for the environmental screening effects on band structures^{38,39}. We then applied the GW corrections to the ground-state density functional theory (DFT) eigenvalues of WSe_2 and SnS_2 from explicit heterobilayer and vdW superlattices (see Methods for details). The atomic structure and the calculated differential charge density of the bilayer vdW heterostructure and the periodic vdW superlattice are shown in Extended Data Fig. 2b, c and Fig. 3a, respectively. The calculation shows that the $\text{SnS}_2/\text{WSe}_2$ heterobilayer exhibits a type-II band alignment with the valence band maximum (VBM) coming entirely from the K point of WSe_2 , and with the conduction band minimum (CBM) from the M point of SnS_2 , resulting in an apparent indirect bandgap of 0.33 eV (Fig. 3b). By contrast, in the vdW superlattice, the WSe_2 VBM is elevated, whereas the CBM of the SnS_2 is lowered, resulting in a type-III band alignment with -0.43 eV band offset, thus changing the band profile from mostly semiconducting characteristics in heterobilayers to metallic behaviour in vdW superlattices (Fig. 3c).

Photoluminescence studies reveal an apparent redshift of the WSe_2 photoluminescence peak from 771 nm in monolayer WSe_2 , to 780 nm in the $\text{SnS}_2/\text{WSe}_2$ heterobilayer and 815 nm in the $\text{SnS}_2/\text{WSe}_2$ vdW superlattice, along with a substantial photoluminescence quench in the roll-up vdW superlattice (Extended Data Fig. 3a), which can be attributed to the change of the relative band alignment and the dielectric environment upon rolling up⁴⁰. Additionally, Raman spectroscopy studies show that the relative intensity of the out-of-plane A_{1g} resonance mode at 309 cm^{-1} for SnS_2 is enhanced in the vdW superlattices compared with that in the heterobilayers (Extended Data Fig. 3b), similarly to the

enhanced A_{1g} mode in bulk SnS_2 compared with monolayer SnS_2 (ref. ⁴¹). Such Raman evolution with formation of vdW superlattices indicates intimate interlayer vdW interaction between the neighbouring layers within vdW superlattices (similar to that in bulk layered crystals).

To examine the electrical transport properties of the vdW superlattices, we fabricated field-effect transistors (FETs) from the $\text{SnS}_2/\text{WSe}_2$ heterobilayers and the $\text{SnS}_2/\text{WSe}_2$ roll-up vdW superlattices on a SiO_2/Si substrate, with Cr/Au thin films as the source and drain electrodes, a Si substrate as the back gate, and 285 nm of SiO_2 as the gate dielectric (Extended Data Fig. 4a, b), and conducted electrical transport studies. At zero gate voltage, the output characteristic (drain–source current I_{ds} versus drain–source voltage V_{ds}) of the $\text{SnS}_2/\text{WSe}_2$ heterobilayer device shows little conduction, whereas that of the $\text{SnS}_2/\text{WSe}_2$ roll-up vdW superlattice shows high conductance with a current of the order of 100 μA at 1 V bias (Fig. 3d). The transfer characteristic (I_{ds} – V_{gs} , where V_{gs} is the gate–source voltage) of the $\text{SnS}_2/\text{WSe}_2$ heterobilayer FET shows ambipolar behaviour, which is largely attributed to the p-type nature of WSe_2 and the n-type nature of SnS_2 , whereas the $\text{SnS}_2/\text{WSe}_2$ roll-up vdW superlattice shows a relatively small tunability and weak p-type characteristics (Fig. 3e). The transfer characteristics also show that the I_{ds} value of the vdW superlattice at zero gate voltage is over five orders of magnitude larger than that of the heterobilayer vdW heterostructure at zero gate voltage. Measurements of over 60 devices consistently show that the overall current of the $\text{SnS}_2/\text{WSe}_2$ vdW superlattice FETs is about 2–6 orders of magnitude larger than that of the heterobilayer FETs at zero gate voltage (Fig. 3f), highlighting the greatly improved charge transport in the roll-up vdW superlattices due to the substantially reduced bandgap. On the basis of the transfer characteristics, we can also derive the carrier mobility and carrier density in the corresponding heterobilayer vdW heterostructures and roll-up vdW superlattices (see Methods, Extended Data Fig. 4a–d). Notably, the $\text{SnS}_2/\text{WSe}_2$ roll-up vdW superlattices show a carrier density exceeding 10^{20} cm^{-3} , about 2–3 orders of magnitude higher than that in the $\text{SnS}_2/\text{WSe}_2$ heterobilayers at the same gate voltage, consistent with the band structure evolution

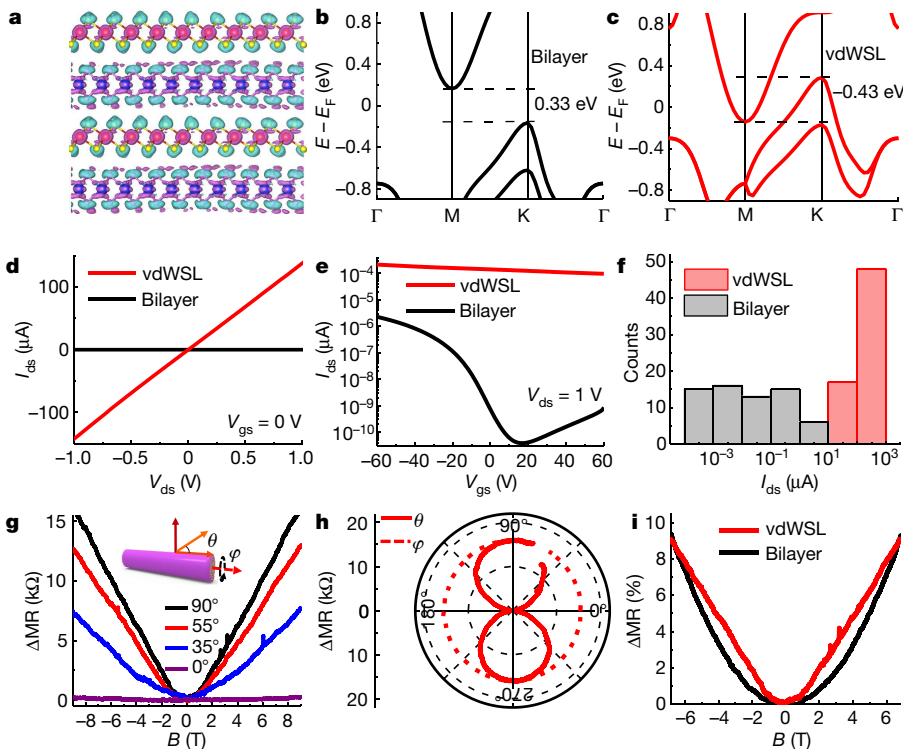


Fig. 3 | Electrical transport and magnetotransport properties of the SnS₂/WSe₂ roll-up vdW superlattices. **a**, Atomic structure and differential charge density calculated for the SnS₂/WSe₂ vdW superlattice. The amaranth and blue isosurfaces represent negative and positive charge density differences, respectively, between the vdW superlattice and the separated layers. The isosurface value is chosen as 0.0005 e au⁻³ (*e*, elementary charge; *au*, atomic unit). **b**, Calculated band structure of SnS₂/WSe₂ heterobilayer (*E*, Fermi level). **c**, Calculated band structure of SnS₂/WSe₂ vdW superlattice (vdWSL). **d**, Output characteristics of the SnS₂/WSe₂ roll-up FET and the SnS₂/WSe₂ heterobilayer FET at *V*_{gs} = 0 V. **e**, Transfer characteristics of the SnS₂/WSe₂ roll-up FET and the

SnS₂/WSe₂ heterobilayer FET at *V*_{ds} = 1 V. **f**, Statistical distribution of the output current at *V*_{ds} = 1 V and *V*_{gs} = 0 V, highlighting that the SnS₂/WSe₂ roll-up FETs show considerably higher conductance than the heterobilayers. **g**, Magnetoresistance (ΔMR) of roll-up vdW superlattices with different rotation angles θ at T = 3 K. Inset, schematic drawing of the roll-up vdW superlattices, and definition of θ and φ . **h**, Angle-dependent magnetoresistance of the SnS₂/WSe₂ roll-up vdW superlattice at 9 T. **i**, Comparison of the magnetoresistance of the SnS₂/WSe₂ roll-up vdW superlattice and the SnS₂/WSe₂ heterobilayer at T = 3 K, showing a linear dependence on the magnetic field for the roll-up and a quadratic dependence for the heterobilayer.

from a largely type-II band alignment to a type-III band alignment upon rolling up, as predicted by the GW calculations (Fig. 3a–c).

A notable difference between the heterobilayer vdW heterostructures and the roll-up vdW superlattices is that the dimensionality of the studied system changes from 2D to 1D upon rolling up. The 1D transport nature of the roll-ups can be confirmed by angle-dependent magnetoresistance studies. To this end, we conducted magnetoresistance studies of the SnS₂/WSe₂ vdW superlattice at various rotation angles and temperatures. Specifically, we define θ is the rotation angle along the roll-ups and φ as the rotation angle perpendicular to the roll-ups (Fig. 3g inset). Because of the rotational symmetry of the 1D roll-up around φ , the magnetoresistance should only depend on θ . In Fig. 3g, we plot the magnetoresistance as a function of the magnetic field B at different θ values; for every field the magnitude of the magnetoresistance decreases as θ is reduced. Notably, both the shape and the amplitude agree well with those taken at different θ values after normalizing to $B \sin \theta$ (Extended Data Fig. 4e). The magnetoresistance as a function of both θ and φ at B = 9 T (Fig. 3h) exhibits a sine function dependence of θ , but does not vary with φ , consistent with the 1D transport characteristic expected for the roll-up vdW superlattices.

Furthermore, the magnetoresistance of the 1D roll-ups exhibits a clear linear relationship with the magnetic field at 3 K, whereas the magnetoresistance of the 2D vdW heterostructures shows a quadratic dependence on the magnetic field (Fig. 3i). The quadratic magnetoresistance dependence is typically observed in other 1D and 2D systems, such as antimony nanowires and GaAs 2D electron gas⁴², and usually originates from the Onsager reciprocity relation⁴³. The linear

magnetoresistance has been previously attributed to the topological nature of the band profile, which exists in gapless semiconductors such as graphene and some other topological insulators such as Bi₂Te₃ (ref. ⁴⁴). However, the Chern number from first-principles calculations^{45,46} is nearly zero for both the heterobilayers and the roll-up vdW superlattices, which may imply that other possible mechanisms beyond non-trivial topology are probably responsible for the linear magnetoresistance^{47,48}.

The rolling-up strategy for vdW superlattice assembly is general and may be extended to produce diverse 2D/2D vdW superlattice roll-ups, including NbSe₂/MoSe₂, MoS₂/WS₂, MoSe₂/WSe₂, SnS₂/MoS₂, Cr₅Te₈/WSe₂, SnSe₂/WSe₂ and In₂Se₃/WSe₂ vdW superlattices, (Fig. 4a, Extended Data Fig. 5). These 2D/2D roll-up vdW superlattices with distinct chemical compositions and physical properties offer a rich platform for investigating ferroelectricity, ferromagnetism, superconductivity and piezoelectricity under different geometries and dimensionalities.

Furthermore, more complex 2D/2D/2D roll-up vdW superlattices with three distinct constituent materials (for example, SnS₂/MoS₂/WS₂) could also be obtained using a similar approach (Fig. 4b). STEM (Fig. 4g) and EDS mapping (Fig. 4h) images clearly reveal a high-order superlattice structure consisting of a repeating unit of monolayer WS₂, monolayer MoS₂ and bilayer SnS₂, which is further confirmed by the integrated intensity profiles for W, Mo and Sn (Fig. 4i). The statistical histogram of the peak-to-peak separations of W in the STEM image shows a rather narrow distribution of 2.50 ± 0.01 nm (Fig. 4j), demonstrating the formation of a highly uniform superlattice structure for

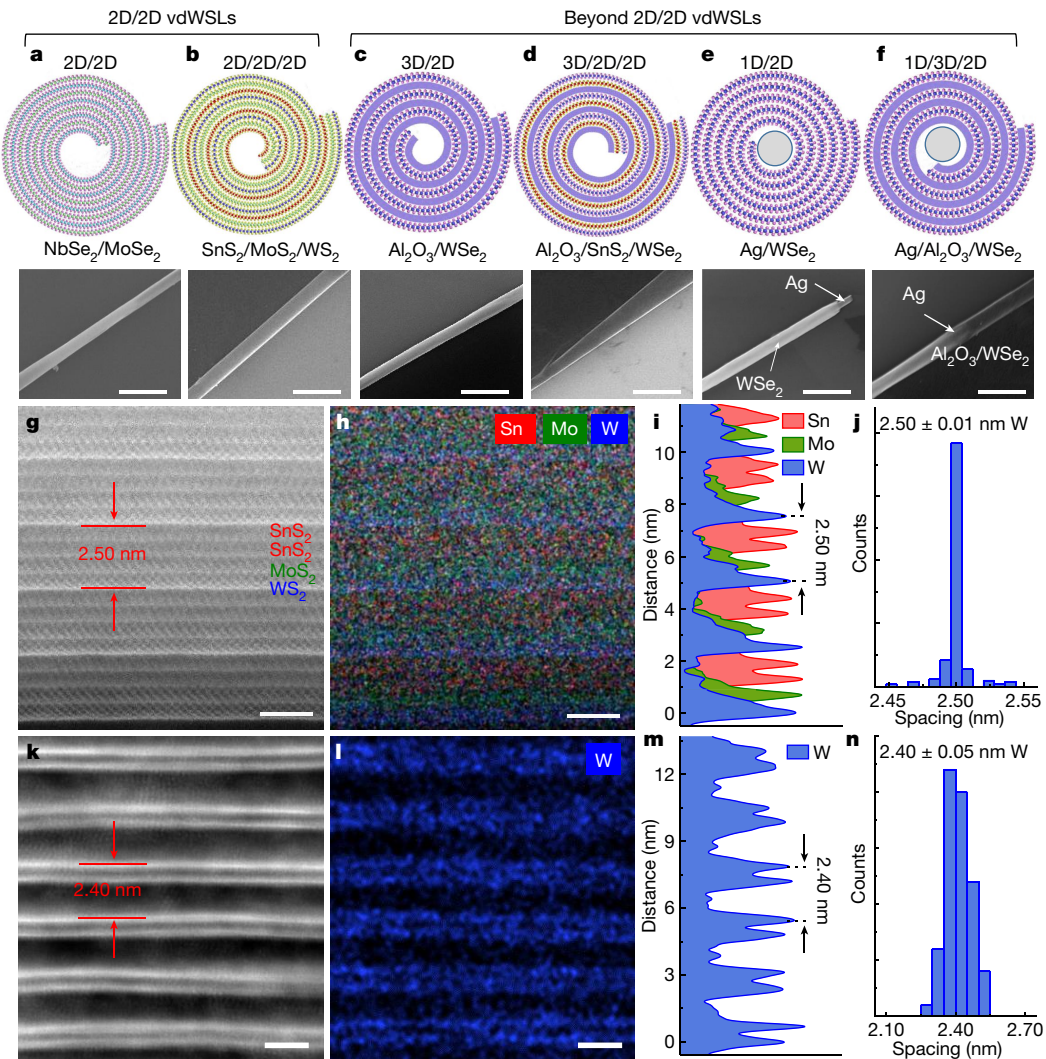


Fig. 4 | Multi-dimensional roll-up vdW superlattices. **a, b**, Schematic cross-sectional views (top) and SEM images (bottom) of 2D/2D ($\text{NbSe}_2/\text{MoSe}_2$) vdW superlattice (**a**) and 2D/2D/2D ($\text{SnS}_2/\text{MoS}_2/\text{WS}_2$) vdW superlattice (**b**). Scale bars, 1 μm . **c–f**, Schematic cross-sectional views (top) and SEM images (bottom) of roll-up vdW superlattices beyond 2D/2D: 3D/2D ($\text{Al}_2\text{O}_3/\text{WSe}_2$) vdW superlattice (**c**); 3D/2D/2D ($\text{Al}_2\text{O}_3/\text{SnS}_2/\text{WS}_2$) vdW superlattice (**d**); 1D/2D (Ag/WSe_2) vdW superlattice (**e**); 1D/3D/2D ($\text{Ag}/\text{Al}_2\text{O}_3/\text{WSe}_2$) vdW superlattice (**f**). Scale bars, 1 μm . **g**, STEM image of $\text{SnS}_2/\text{MoS}_2/\text{WS}_2$ vdW superlattice. Scale bar, 2 nm. **h**, EDS mapping image of W (blue), Mo (green) and Sn (red). Scale bar, 2 nm. **i**, Integrated EDS intensity profile for W, Mo and Sn. **j**, Statistical distribution of interlayer spacing between W atoms in **g**. **k**, Cross-sectional STEM image of $\text{Al}_2\text{O}_3/\text{WSe}_2$ vdW superlattice. Scale bar, 2 nm. **l**, EDS mapping image of W (blue). Scale bar, 2 nm. **m**, Integrated EDS intensity profile for W. **n**, Statistical distribution of superlattice periodicity between W atoms in **k**.

the three 2D materials. In comparison with recently reported 1D vdW heterostructures containing three different concentric monolayers obtained through a sequential-synthesis process⁴⁹, our roll-up vdW superlattices have a radially winding structure with many more repeating units to form high-order superlattices that are difficult to achieve through the sequential-growth process.

Beyond typical 2D materials, the same approach can be extended to include 3D bulk thin-film materials or 1D nanowires to create mixed-dimensional vdW superlattices, such as 3D/2D ($\text{Al}_2\text{O}_3/\text{WSe}_2$), 3D/2D/2D ($\text{Al}_2\text{O}_3/\text{SnS}_2/\text{WSe}_2$), 1D/2D (Ag nanowire/ WSe_2) and 1D/3D/2D (Ag nanowire/ $\text{Al}_2\text{O}_3/\text{WSe}_2$) vdW superlattices (Fig. 4c–f; see Methods for details). For example, by using atomic layer deposition (ALD) to deposit a thin layer of Al_2O_3 on bilayer WSe_2 , followed by a similar rolling-up process, an $\text{Al}_2\text{O}_3/\text{WSe}_2$ 3D/2D vdW superlattice is obtained (Fig. 4c). The STEM image, EDS mapping image and the line profiles of the $\text{Al}_2\text{O}_3/\text{WSe}_2$ vdW superlattice clearly reveal the superlattice structure, consisting of repeating units of bilayer WSe_2 and 1.2-nm-thick Al_2O_3 (Fig. 4k–m). The statistical distribution shows a consistent interlayer periodicity of 2.40 ± 0.05 nm (Fig. 4n). We note that the standard deviation observed in 3D/2D vdW superlattices is apparently larger than that in 2D/2D vdW superlattices, which may be attributed to the finite surface/interface roughness of the Al_2O_3 layer (when compared with the atomically smooth 2D crystals). Moreover, photoluminescence spectroscopic studies show a slight redshift upon the formation of $\text{Al}_2\text{O}_3/\text{WSe}_2$ vdW superlattices (Extended Data Fig. 6), which may be attributed to the change of the dielectric environment upon rolling up⁵⁰.

Additionally, more complex 3D/2D/2D vdW superlattice ($\text{Al}_2\text{O}_3/\text{SnS}_2/\text{WSe}_2$ vdW superlattice) can be prepared by rolling up the $\text{SnS}_2/\text{WSe}_2$ heterobilayer with an ALD-grown Al_2O_3 layer (Fig. 4d). Taking a step further, by first placing a Ag nanowire on the WSe_2 nanosheet, followed by a rolling-up process, a 1D/2D (Ag/WSe_2) roll-up can be obtained with the Ag nanowire wrapped in the centre (Fig. 4e). By placing the Ag nanowire on the WSe_2 nanosheet with an Al_2O_3 layer, followed by a rolling-up process, a 1D/3D/2D roll-up vdW superlattice ($\text{Ag}/\text{Al}_2\text{O}_3/\text{WSe}_2$ vdW superlattice) can also be prepared (Fig. 4f).

Beyond the material compositions, roll-up vdW superlattices with different chiralities (or Eshelby twists) and the associated moiré structures may be obtained, depending on the roll-up angles. Indeed, the electron diffraction patterns show that a series of the roll-up structures with variable chiral angles are obtained in both WSe_2 and $\text{SnS}_2/\text{WSe}_2$ roll-ups⁴⁹ (Extended Data Figs. 7, 8). Additionally, high-resolution STEM and TEM images of a $\text{SnS}_2/\text{WSe}_2$ roll-up show moiré superlattices with a chirality (twist angle from the roll-up axis) consistent with the corresponding roll-up angle determined from the electron diffraction studies (Extended Data Fig. 9). The tuning of chiral angles and the associated moiré patterns could open up another degree of freedom to tailor the electronic structure and develop unconventional chiroptoelectronic properties. Precise control of such chiral angles and investigation of the corresponding physical properties represents an exciting direction to explore in future studies.

In summary, we report a straightforward and general approach to multi-dimensional high-order vdW superlattices consisting of alternating layers of distinct 2D materials and various 3D and 1D materials

with widely variable compositions and dimensions for creating highly engineered artificial materials beyond the reach of traditional material systems. This provides considerable freedom to tailor the interlayer coupling, dimensionality, chirality and topology of the resulting superlattice structures. The formation of such diverse high-order vdW superlattices with designable band offset and chirality enables the rational tuning of the carrier confinement or carrier separation, producing complex superlattice structures resembling those typically used in multi-sheet transistors, quantum tunnelling devices, advanced light-emitting diodes or quantum cascading lasers. In addition, the integration of 1D or 3D components may offer unique geometries for carrier confinement or carrier injection, which is critical for both exploring exotic quantum physics and realizing specific device functions. Our study thus defines a rich material platform for both fundamental studies and technological applications.

Online content

Any methods, additional references, Nature Research reporting summaries, source data, extended data, supplementary information, acknowledgements, peer review information; details of author contributions and competing interests; and statements of data and code availability are available at <https://doi.org/10.1038/s41586-021-03338-0>.

1. Novoselov, K. S., Mishchenko, A., Carvalho, A. & Castro Neto, A. H. 2D materials and van der Waals heterostructures. *Science* **353**, aac9439 (2016).
2. Saito, Y., Nojima, T. & Iwasa, Y. Highly crystalline 2D superconductors. *Nat. Rev. Mater.* **2**, 16094 (2017).
3. Dean, C. R. et al. Boron nitride substrates for high-quality graphene electronics. *Nat. Nanotechnol.* **5**, 722–726 (2010).
4. Haigh, S. J. et al. Cross-sectional imaging of individual layers and buried interfaces of graphene-based heterostructures and superlattices. *Nat. Mater.* **11**, 764–767 (2012).
5. Geim, A. K. & Grigorieva, I. V. Van der Waals heterostructures. *Nature* **499**, 419–425 (2013).
6. Liu, Y. et al. Van der Waals heterostructures and devices. *Nat. Rev. Mater.* **1**, 16042 (2016).
7. Kang, K. et al. Layer-by-layer assembly of two-dimensional materials into wafer-scale heterostructures. *Nature* **550**, 229–233 (2017).
8. Britnell, L. et al. Field-effect tunneling transistor based on vertical grapheme heterostructures. *Science* **335**, 947–950 (2012).
9. Yu, W. J. et al. Vertically stacked multi-heterostructures of layered materials for logic transistors and complementary inverters. *Nat. Mater.* **12**, 246–252 (2013).
10. Yu, W. J. et al. Highly efficient gate-tunable photocurrent generation in vertical heterostructures of layered materials. *Nat. Nanotechnol.* **8**, 952–958 (2013).
11. Fang, H. et al. Strong interlayer coupling in van der Waals heterostructures built from single-layer chalcogenides. *Proc. Natl Acad. Sci. USA* **111**, 6198–6202 (2014).
12. Lee, C. H. et al. Atomically thin p-n junctions with van der Waals heterointerfaces. *Nat. Nanotechnol.* **9**, 676–681 (2014).
13. Withers, F. et al. Light-emitting diodes by band-structure engineering in van der Waals heterostructures. *Nat. Mater.* **14**, 301–306 (2015).
14. Rivera, P. et al. Valley-polarized exciton dynamics in a 2D semiconductor heterostructure. *Science* **351**, 688–691 (2016).
15. Klein, D. R. et al. Probing magnetism in 2D van der Waals crystalline insulators via electron tunneling. *Science* **360**, 1218–1222 (2018).
16. Cao, Y. et al. Unconventional superconductivity in magic-angle graphene superlattices. *Nature* **556**, 43–50 (2018).
17. Bae, S. H. et al. Integration of bulk materials with two-dimensional materials for physical coupling and applications. *Nat. Mater.* **18**, 550–560 (2019).
18. Sutter, P., Wimer, S. & Sutter, E. Chiral twisted van der Waals nanowires. *Nature* **570**, 354–357 (2019).
19. Kim, K. K., Lee, H. S. & Lee, Y. H. Synthesis of hexagonal boron nitride heterostructures for 2D van der Waals electronics. *Chem. Soc. Rev.* **47**, 6342–6369 (2018).
20. Chen, P., Zhang, Z. W., Duan, X. D. & Duan, X. F. Chemical synthesis of two-dimensional atomic crystals, heterostructures and superlattices. *Chem. Soc. Rev.* **47**, 3129–3151 (2018).
21. Zhao, M. et al. Large-scale chemical assembly of atomically thin transistors and circuits. *Nat. Nanotechnol.* **11**, 954–959 (2016).
22. Duan, X. et al. Lateral epitaxial growth of two-dimensional layered semiconductor heterojunctions. *Nat. Nanotechnol.* **9**, 1024–1030 (2014).
23. Gong, Y. J. et al. Vertical and in-plane heterostructures from WS₂/MoS₂ monolayers. *Nat. Mater.* **13**, 1135–1142 (2014).
24. Huang, C. et al. Lateral heterojunctions within monolayer MoSe₂–WSe₂ semiconductors. *Nat. Mater.* **13**, 1096–1101 (2014).
25. Shi, Y. M., Li, H. N. & Li, L.-J. Recent advances in controlled synthesis of two-dimensional transition metal dichalcogenides via vapour deposition techniques. *Chem. Soc. Rev.* **44**, 2744–2756 (2015).
26. Yu, Y. F. et al. Equally efficient interlayer exciton relaxation and improved absorption in epitaxial and nonepitaxial MoS₂/WS₂ heterostructures. *Nano Lett.* **15**, 486–491 (2015).
27. Zhang, J. et al. Observation of strong interlayer coupling in MoS₂/WS₂ heterostructures. *Adv. Mater.* **28**, 1950–1956 (2016).
28. Yang, T. F. et al. Van der Waals epitaxial growth and optoelectronics of large-scale WSe₂/SnS₂ vertical bilayer p–n junctions. *Nat. Commun.* **8**, 1906 (2017).
29. Li, F. et al. Rational kinetics control toward universal growth of 2D vertically stacked heterostructures. *Adv. Mater.* **31**, 1901351 (2019).
30. Zhang, Z. et al. Robust epitaxial growth of two-dimensional heterostructures, multiheterostructures, and superlattices. *Science* **357**, 788–792 (2017).
31. Sahoo, P. K., Memaran, S., Xin, Y., Balicas, L. & Gutiérrez, H. R. One-pot growth of two-dimensional lateral heterostructures via sequential edge-epitaxy. *Nature* **553**, 63–67 (2018).
32. Xie, S. et al. Coherent, atomically thin transition-metal dichalcogenide superlattices with engineered strain. *Science* **359**, 1131–1136 (2018).
33. Wang, C. et al. Monolayer atomic crystal molecular superlattices. *Nature* **555**, 231–236 (2018).
34. Zhang, Z. W. et al. Ultrafast growth of large single crystals of monolayer WS₂ and WSe₂. *Natl. Sci. Rev.* **7**, 737–744 (2020).
35. Halim, U. et al. A rational design of cosolvent exfoliation of layered materials by directly probing liquid–solid interaction. *Nat. Commun.* **4**, 2213 (2013).
36. Cui, X. et al. Rolling up transition metal dichalcogenide nanoscrolls via one drop of ethanol. *Nat. Commun.* **9**, 1301 (2018).
37. Ping, Y., Rocca, D. & Galli, G. Electronic excitations in light absorbers for photoelectrochemical energy conversion: first principles calculations based on many body perturbation theory. *Chem. Soc. Rev.* **42**, 2437–2469 (2013).
38. Yan, J., Thygesen, K. S. & Jacobsen, K. W. Nonlocal screening of plasmons in graphene–semiconducting and metallic substrates: first-principles calculations. *Phys. Rev. Lett.* **106**, 146803 (2011).
39. Ugeda, M. M. et al. Giant bandgap renormalization and excitonic effects in a monolayer transition metal dichalcogenide semiconductor. *Nat. Mater.* **13**, 1091–1095 (2014).
40. Zeng, H. L. et al. Optical signature of symmetry variations and spin–valley coupling in atomically thin tungsten dichalcogenides. *Sci. Rep.* **3**, 1608 (2013).
41. Gonzalez, J. M. & Oleynik, I. I. Layer-dependent properties of SnS₂ and SnSe₂ two-dimensional materials. *Phys. Rev. B* **94**, 125443 (2016).
42. Heremans, J., Thrush, C. M., Lin, Y. M., Cronin, S. B. & Dresselhaus, M. S. Transport properties of antimony nanowires. *Phys. Rev. B* **63**, 085406 (2001).
43. Onsager, L. Reciprocal relations in irreversible processes I. *Phys. Rev.* **37**, 405–426 (1931).
44. Wang, X. L., Du, Y., Dou, S. X. & Zhang, C. Room temperature giant and linear magnetoresistance in topological insulator Bi₂Te₃ nanosheets. *Phys. Rev. Lett.* **108**, 266806 (2012).
45. Wang, X. J., Yates, J. R., Souza, I. & Vanderbilt, D. Ab initio calculation of the anomalous Hall conductivity by Wannier interpolation. *Phys. Rev. B* **74**, 195118 (2006).
46. Qiao, Z. H. et al. Quantum anomalous Hall effect in graphene proximity coupled to an antiferromagnetic insulator. *Phys. Rev. Lett.* **112**, 116404 (2014).
47. Khouri, T. et al. Linear magnetoresistance in a quasi-free two-dimensional electron gas in an ultrahigh mobility GaAs quantum well. *Phys. Rev. Lett.* **117**, 256601 (2016).
48. Xiao, C. et al. Linear magnetoresistance induced by intra-scattering semiclassics of Bloch electrons. *Phys. Rev. B* **101**, 201410 (2020).
49. Xiang, R. et al. One-dimensional van der Waals heterostructures. *Science* **367**, 537–542 (2020).
50. Guo, C. H., Xu, J. Q., Rocca, D. & Ping, Y. Substrate screening approach for quasiparticle energies of two-dimensional interfaces with lattice mismatch. *Phys. Rev. B* **102**, 205113 (2020).

Publisher's note Springer Nature remains neutral with regard to jurisdictional claims in published maps and institutional affiliations.

© The Author(s), under exclusive licence to Springer Nature Limited 2021

¹Hunan Key Laboratory of Two-Dimensional Materials, State Key Laboratory for Chemo/Biosensing and Chemometrics, College of Chemistry and Chemical Engineering, Hunan University, Changsha, China. ²Department of Chemistry and Biochemistry, University of California Los Angeles, Los Angeles, CA, USA. ³School of Physics and Electronics, Hunan University, Changsha, China. ⁴Department of Chemistry and Biochemistry, University of California Santa Cruz, Santa Cruz, CA, USA. ⁵Department of Materials Science and Engineering, University of California Los Angeles, Los Angeles, CA, USA. ⁶Department of Materials Science and Engineering, University of California Irvine, Irvine, CA, USA. ⁷Beijing Key Laboratory of Green Chemical Reaction Engineering and Technology, Department of Chemical Engineering, Tsinghua University, Beijing, China. ⁸State Key Laboratory for Advanced Metals and Materials, School of Materials Science and Engineering, University of Science and Technology Beijing, Beijing, China. ⁹Sustainable Energy Technologies Centre, College of Engineering, King Saud University, Riyadh, Saudi Arabia. ¹⁰Mechanical Engineering Department, College of Engineering, King Saud University, Riyadh, Saudi Arabia. ¹¹Beijing Advanced Innovation Center for Materials Genome Engineering, Beijing Key Laboratory for Advanced Energy Materials and Technologies, University of Science and Technology Beijing, Beijing, China. ¹²Department of Physics and Astronomy, University of California Irvine, Irvine, CA, USA. ¹³California NanoSystems Institute, University of California Los Angeles, Los Angeles, CA, USA. ¹⁴These authors contributed equally: Bei Zhao, Zhong Wan.

[✉]e-mail: xidongduan@hnu.edu.cn; xduan@chem.ucla.edu

Methods

CVD growth of WSe₂ and MoS₂ monolayers

The WSe₂ monolayers were grown with a reverse-flow reactor in a one-zone tube furnace (Tianjin Zhonghuan Furnace) to ensure uniform nucleation and growth^{30,34}. The WSe₂ powder (-99.99%; Alfa Aesar) was placed in a quartz boat at the central heating zone of the furnace, and the SiO₂/Si substrate was placed in the downstream zone of the furnace. Before heating, the system was purged with 1,215 standard cubic centimetres per minute (sccm) Ar (-99.999%) for 5 min to eliminate oxygen and moisture in the furnace. The WSe₂ powder was heated to 1,185 °C in 40 min under ambient pressure with a reverse flow of 80 sccm Ar (-99.999%), and then the chemical vapour source was carried downstream by a forward flow of 80 sccm Ar for growth for 2 min under ambient pressure. After the reaction, the chamber was cooled to room temperature naturally.

The MoS₂ monolayers were grown using a one-zone CVD system. A Mo precursor was prepared by spin-coating Na₂MoO₄ solution (40 mg in 10 ml of water; 99%; Macklin) onto the SiO₂/Si substrate, which was placed in a quartz boat at the centre of the furnace. Another quartz boat with S powder (0.1 g; 99.99%; Alfa Aesar) was placed outside the furnace. After purging the system with 1,215 sccm Ar flow for 5 min, the Mo precursor was heated to 830 °C in 22 min under a forward flow of 60 sccm Ar. The quartz boat with the S powder was then positioned into the upstream hot zone (approximately 240 °C) using a magnet-activated motion system²², and reacted for 3 min to obtain MoS₂ monolayers. After the reaction, the chamber was cooled to room temperature naturally.

CVD growth of SnS₂/WSe₂, SnS₂/MoS₂, In₂Se₃/WSe₂, SnSe₂/WSe₂ and Cr₅Te₈/WSe₂ heterostructures

The SnS₂/WSe₂ heterobilayers were prepared by vdW epitaxial growth of SnS₂ on a WSe₂ substrate in a two-step process using a one-zone tube furnace. First, a SiO₂/Si substrate with WSe₂ nanosheets was prepared by the CVD method described earlier. Next, a quartz boat with S powder (0.1 g; 99.99%; Alfa Aesar) was placed in the upstream zone of the furnace. Another quartz boat with SnO₂ powder (0.06 g; 99%; Macklin) was placed in the centre of the furnace. The substrate with the WSe₂ nanosheets was tilted above the SnO₂ powder. After purging the system with 1,215 sccm Ar for 5 min, the SnO₂ powder was heated to 590 °C (with the temperature of the S powder reaching roughly 180 °C) in 15 min and held at that temperature for 7 min under a forward flow of 80 sccm Ar. Finally, the reaction chamber was rapidly cooled to room temperature by opening the furnace under a forward flow of 80 sccm Ar.

The SnS₂/MoS₂ heterobilayers were grown by the same two-step procedure using the pre-grown MoS₂ as the substrate.

The In₂Se₃/WSe₂ heterobilayers were obtained by vdW epitaxial growth of In₂Se₃ on a WSe₂ substrate using a similar two-step process. In brief, a quartz boat with Se powder (0.2 g; 99.99%; Alfa Aesar) was placed in the upstream zone of the furnace, and another quartz boat with In₂O₃ powder (0.1 g; 99%; Macklin) was placed in the central heating zone of the furnace. The substrate with the WSe₂ nanosheets was tilted above the In₂O₃ powder. After purging with 1,215 sccm Ar flow for 5 min, the In₂O₃ powder was heated to 610 °C (with the temperature of the Se powder reaching roughly 320 °C) in 15 min and held at that temperature for 20 min under a forward flow of 80 sccm Ar and 5 sccm H₂. Finally, the reaction chamber was rapidly cooled to room temperature by opening the furnace.

The SnSe₂/WSe₂ heterobilayers were obtained by vdW epitaxial growth of SnSe₂ on a WSe₂ substrate in a two-step process. In brief, a quartz boat with Se powder (0.2 g; 99.99%; Alfa Aesar) was placed in the upstream zone of the furnace, and another quartz boat with SnO₂ powder (0.1 g; 99%; Macklin) was placed in the central heating zone of the furnace. A substrate with pre-grown WSe₂ nanosheets was placed in the downstream zone of the furnace. After purging with 1,215 sccm

Ar flow for 5 min, the SnO₂ powder was heated to 600 °C (with the temperature of the Se powder reaching roughly 300 °C) in 15 min and held at that temperature for 15 min under a flow of 70 sccm Ar and 5 sccm H₂. Finally, the reaction chamber was rapidly cooled to room temperature by opening the furnace.

The Cr₅Te₈/WSe₂ heterostructures were prepared by vdW epitaxial growth of Cr₅Te₈ on a WSe₂ substrate using a two-zone tube furnace. A quartz boat with Te powder (0.03 g; 99.99%; Macklin) was placed in the upstream heating zone of the furnace. Another quartz boat with CrCl₃ powder (0.03 g; 99.9%; Alfa Aesar) was placed in the downstream heating zone of the furnace, and a SiO₂/Si substrate with WSe₂ nanosheets was placed on top of the CrCl₃ powder. After purging the system with 1,215 sccm Ar flow for 5 min, the Te powder was heated to 630 °C and the CrCl₃ powder was heated to 645 °C in 25 min under a forward flow of 40 sccm Ar and 30 sccm H₂. The growth was carried out for 4 min at those temperatures before the reaction chamber was rapidly cooled to room temperature by opening the furnace.

CVD growth of MoS₂/WS₂, MoSe₂/WSe₂ and NbSe₂/MoSe₂ heterobilayers

The MoS₂/WS₂ heterobilayers were grown by a one-pot method^{51,52}. The Mo/W precursors were prepared by spin-coating the solution mixture of Na₂MoO₄ (20 mg; 99%; Macklin) and Na₂WO₄·H₂O (30 mg; 99.5%; Macklin) in 10 ml of water onto the SiO₂/Si substrate, which was loaded into a quartz boat and placed in the central heating zone of the furnace. Another quartz boat with S powder (0.1 g; 99.99%; Alfa Aesar) was placed outside the furnace. After purging the system with 1,215 sccm Ar flow for 5 min, the Mo/W precursors were heated to 840 °C in 22 min under a forward flow of 60 sccm Ar. The quartz boat with the S powder was then positioned into the upstream hot zone (approximately 240 °C) of the tube using a magnet-activated motion system²², and reacted for 3 min to obtain a MoS₂/WS₂ bilayer before the chamber was cooled to room temperature naturally.

The MoSe₂/WSe₂ heterobilayers were grown using a two-zone tube furnace and a one-pot method. A quartz boat with Se powder (0.1 g; 99.99%; Alfa Aesar) was placed in the upstream heating zone of the furnace. The Mo/W precursors, prepared by spin-coating a solution mixture of Na₂MoO₄ and Na₂WO₄·H₂O, were placed in a quartz boat in the downstream heating zone of the furnace. After purging the system with 1,215 sccm Ar for 5 min, the Mo/W precursors were heated to 800 °C in 15 min, and the Se powder was heated to 400 °C under a forward flow of 80 sccm Ar and 2 sccm H₂. The reaction lasted for 10 min to obtain MoSe₂/WSe₂ bilayers, before the chamber was cooled to room temperature naturally.

The NbSe₂/MoSe₂ bilayers were grown by the same procedure used for the MoSe₂/WSe₂ bilayer. The solution mixture used to prepare the Nb/Mo precursors contained C₆H₄NNbO_x·nH₂O (60 mg; 99.9%; Macklin) and Na₂MoO₄ (20 mg; 99%; Macklin) in 10 ml of water.

CVD growth of SnS₂/MoS₂/WS₂ heterostructures

The SnS₂/MoS₂/WS₂ heterostructures were grown by vdW epitaxial growth of SnS₂ on pre-grown MoS₂/WS₂ heterobilayers, following a similar procedure as that used for the vdW epitaxial growth of SnS₂ on WSe₂.

ALD growth of Al₂O₃/WSe₂ heterostructures

The Al₂O₃/WSe₂ heterostructures were synthesized by the ALD (TALD-100A) deposition of Al₂O₃ film on pre-grown WSe₂ nanosheets (on SiO₂/Si substrate) at 250 °C using H₂O and trimethylaluminum (Al(CH₃)₃) as precursors.

Fabrication of roll-up vdW superlattices

Initially, an ethanol aqueous solution (volume ratio of ethanol:water = 1:3) is slowly dropped onto the inclined surface of various nanoscale materials/2D/SiO₂/Si substrate to allow the solution to intercalate

Article

between the 2D heterostructure and the SiO_2 interface. The intercalation of solvent molecules delaminates the 2D heterostructures from the substrate, and the capillary force drives the spontaneous rolling-up process to form the corresponding roll-ups. Finally, the roll-ups are dried with an Ar flow. Considering that the 2D layers feature a fully saturated surface bonding structure and do not have a strong interaction with the underlying SiO_2 substrate, the rolling-up process is dictated by the solid–liquid (SiO_2 –solvent) interfacial energy, the surface tension and the evaporation rate. Once the solvent molecules have entered from one edge into the SiO_2 /2D interface, the continued penetration/intercalation of solvent molecules into the interface (capillary force) drives the delamination of 2D layers. In general, the easiness in intercalating the liquid in the SiO_2 /2D interface is determined by the solid–liquid (SiO_2 –solvent) interface energy γ_{sl} , which can be expressed using Young's equation, $\gamma_{\text{sl}} = \gamma_{\text{sg}} - \gamma_{\text{lg}} \cos \theta_c$, where γ_{sl} , γ_{sg} and γ_{lg} are the solid–liquid, solid–gas and liquid–gas interfacial energies, respectively, and θ_c is the equilibrium contact angle. Considering that γ_{sg} is independent of the solvent used and acts simply as a constant, γ_{sl} is minimized when the adhesion tension $\gamma_{\text{lg}} \cos \theta_c$ is maximized. A systematic analysis of the adhesion tension $\gamma_{\text{lg}} \cos \theta_c$ of the ethanol–water solution to the substrate suggests that the solid–liquid interfacial energy is minimized at an ethanol:water ratio of ~1:3 (ref. ³⁵). Therefore, such a mixed solvent would be most readily intercalated between the SiO_2 /2D interface to initiate the delamination process. Additionally, for the capillary-force-driven rolling-up process, a reasonable solvent surface tension, the wettability of the 2D material, as well as the evaporation rate are also important for preventing the solvent from beading up and ensuring a uniform capillary force (along the rolling-up axis) for the rolling-up process. Pure water has too large surface tension and easily beads up during the evaporation stage, and thus cannot drive uniform rolling up. Pure ethanol evaporates too fast and does not allow sufficient time for the rolling-up process to occur, often resulting in wrinkled sheets instead of uniform roll-ups. Therefore, an ethanol:water \approx 1:3 solvent is preferred also for a more uniform and more controllable rolling-up process.

Although the ethanol–water mixture can effectively drive the rolling-up process, our studies show that this is not always successful, and often leaves a peripheral residue on the surface (Extended data Fig. 10a), indicating that the edges of the 2D nanosheets are more tightly bonded with the substrate. This is not surprising, considering that dangling bonds at the edges of 2D sheets may form disordered bonding with the substrate or adsorb some small particles, which could pin the edges more tightly to the substrate compared with the planar regions, where there are no surface dangling bonds. Consequently, the weak capillary force that drives the rolling-up process may not be strong enough to completely peel off the edges to form clean roll-ups. Adding ~5% $\text{NH}_3 \cdot \text{H}_2\text{O}$ into the ethanol–water mixture can help to better release the edge from the substrate and achieve more complete roll-ups (Extended Data Fig. 10b); this is attributed to the slight etching effect to the SiO_2 substrate, which helps to weaken the edge–substrate interaction. Overall, once the planar vdW heterostructures are prepared, the capillary-force-driven rolling-up process is highly reproducible. In general, about 80% of the 2D nanosheets on the substrate spontaneously roll up upon exposure to the ethanol–water mixed solvent, although many roll-ups show only partial rolling up owing to incomplete delamination of the more tightly pinned edges. By introducing 5% ammonia into the mixed solvent to help weaken the edge-pinning effect, about 90 % of the 2D nanosheets show spontaneous rolling up, with ~60% showing complete rolling up (Extended Data Fig. 10c). Overall, our approach is applicable and reproducible for a wide range of 2D/2D (for example, $\text{SnS}_2/\text{WSe}_2$, $\text{NbSe}_2/\text{MoSe}_2$, MoS_2/WS_2 , $\text{MoSe}_2/\text{WSe}_2$, $\text{SnS}_2/\text{MoS}_2$, $\text{Cr}_5\text{Te}_3/\text{WSe}_2$, $\text{SnSe}_2/\text{WSe}_2$ and $\text{In}_2\text{Se}_3/\text{WSe}_2$), 2D/2D/2D ($\text{SnS}_2/\text{MoS}_2/\text{WS}_2$), 3D/2D ($\text{Al}_2\text{O}_3/\text{WSe}_2$), 3D/2D/2D ($\text{Al}_2\text{O}_3/\text{SnS}_2/\text{WSe}_2$), 1D/2D (Ag nanowire/ WSe_2) and 1D/3D/2D (Ag nanowire/ $\text{Al}_2\text{O}_3/\text{WSe}_2$) vdW superlattices.

Characterization

The morphologies of all samples were characterized by optical microscopy (DP27, Olympus), SEM (MIRA3 LMH, Hunan Navi New Materials Technology) and TEM (Titan G2 60-300, Tecnai G2 F20). The Raman and photoluminescence spectra of all samples were characterized by Raman spectroscopy (inVia Reflex, Renishaw with a 488-nm laser as the excitation source). The thickness of all samples was characterized by an atomic force microscope (Bruker Icon). The STEM characterizations and EDS analyses were performed using a Titan Cubed Themis G2 300 STEM instrument (200 keV) and a JEOL JEM-ARM300CF S/STEM system (300 keV).

Band structure calculation

The band structures were computed using many-body perturbation theory and the GW approximation with inputs of the ground-state eigenvalues and wavefunctions from the DFT Perdew–Burke–Ernzerhof (PBE) exchange–correlation functional (G_0W_0 @PBE). We used $10 \times 10 \text{ WSe}_2$ and $9 \times 9 \text{ SnS}_2$ supercells to build bilayer structures and superlattices to obtain minimum lattice mismatch. We note that only with this structural model and level of theory can we include all the important physical effects: the accurate dielectric screening that is necessary to correctly describe the strong layer dependence of the band structure of 2D materials, a minimum strain that is closer to a realistic structure, the interface charge transfer or hybridization, and accurate electron correlations. Previous 2D heterojunction band offsets have been mostly obtained using the natural band offset from monolayer 2D materials in vacuum, which excluded the dielectric screening from the other monolayer 2D material in the heterojunction, and hybridization at interfaces³³. Furthermore, the hybrid functionals that are widely used for bulk semiconductors, such as Heyd–Scuseria–Ernzerhof density functionals³⁴, could not provide the qualitatively correct trend for the layer dependence of the band structure of the 2D materials. However, direct GW calculations for such large systems are computationally formidable. Therefore, we implemented an efficient screening approach for GW corrections to account for environmental screening effects on band structures^{38,39}. We computed the GW corrections for WSe_2 and SnS_2 with their respective dielectric environments and the atomic structure at the heterobilayer and superlattice; then, we applied the GW corrections to the ground-state DFT eigenvalues of WSe_2 and SnS_2 from explicit heterobilayer and vdW superlattice systems. More computational details are provided in the following.

All ground-state DFT calculations were performed using the open-source plane-wave code Quantum ESPRESSO⁵⁵ with ONC norm-conserving pseudopotentials⁵⁶ and a kinetic energy cutoff of 70 Ry for the wavefunctions (1 Ry = 13.605 eV). We used PBE exchange correlation functionals⁵⁷, including self-consistent spin–orbit coupling (SOC) and van der Waals interactions⁵⁸, in all our structural relaxations. $10 \times 10 \text{ WSe}_2$ and $9 \times 9 \text{ SnS}_2$ supercells were used to model the heterostructures. The lattice constant c of the vdW superlattice was obtained by relaxing the primitive cell to be stress-free. For the heterobilayer system, we used 20 Å of vacuum to separate periodic images. A Γ -point calculation was used to provide self-consistent and structure-relaxation calculations of the heterostructure. Convergence tests were performed for all of the aforementioned settings.

To compute the GW corrections on WSe_2 and SnS_2 , including environmental screening in the heterobilayer and the vdW superlattice, we separate both the heterobilayer and the vdW superlattice into two subsystems containing only a WSe_2 layer (subsystem a) and a SnS_2 layer (subsystem b), and the reducible polarizability χ^{tot} of the total system can be approximated as the sum of the effective reducible polarizabilities ($\chi_{\text{eff}}^{\text{a}}, \chi_{\text{eff}}^{\text{b}}$) of the two subsystems³⁸, $\chi^{\text{tot}} = \chi_{\text{eff}}^{\text{a}} + \chi_{\text{eff}}^{\text{b}}$. We implement this formulation into a post-processing code interfacing with the Yambo⁵⁹ code. The cutoff for the dielectric matrix and the GW self-energy is 15 Ry. The number of bands in the GW calculations is set

to 800 (without SOC) for SnS_2 and 1,600 (with SOC) for WSe_2 . We use $27 \times 27 \times 2$ and $30 \times 30 \times 2$ k -grids for the GW calculations of WSe_2 and SnS_2 from the superlattice structure (we keep the same position of atoms and corresponding layer spacings), and $27 \times 27 \times 1$ and $30 \times 30 \times 1$ k -grids for the GW calculations of WSe_2 and SnS_2 from the bilayer structure. A 2D Coulomb truncation is applied for the bilayer system to speed up the vacuum convergence⁶⁰ (20 Å of vacuum is enough for convergence), but not for the superlattice. The numerical parameters in the GW calculations converge within 0.1 eV.

Device fabrication and characterization

The $\text{SnS}_2/\text{WSe}_2$ heterobilayers and $\text{SnS}_2/\text{WSe}_2$ vdW superlattice roll-ups were spin-coated with PMMA and then fabricated by electron-beam lithography, followed by deposition of Cr/Au for the electrical contacts (10 nm Cr/50 nm Au). The electrical performance of the fabricated FETs was measured with a Lake Shore TTPX probe station and an Agilent B1500A semiconductor parameter analyser. The carrier mobility of the $\text{SnS}_2/\text{WSe}_2$ heterobilayers and the $\text{SnS}_2/\text{WSe}_2$ vdW superlattice roll-ups as calculated as $\mu_{2D} = \frac{L}{WV_{ds}C_{2D}} \frac{dI_{ds}}{dV_{gs}}$ and $\mu_{1D} = \frac{L^2}{V_{ds}C_{1D}} \frac{dI_{ds}}{dV_{gs}}$, respectively, where L is the channel length; the channel width of the heterobilayer is defined using the trapezoidal element current model, $W = \frac{W_2 - W_1}{\ln W_2 - \ln W_1}$ (ref. ⁶¹; see Extended Data Fig. 4a for the definition of W_1 and W_2); C_{2D} and C_{1D} are the capacitances for 2D and 1D channel material, respectively, which were calculated as $C_{2D} = \frac{\epsilon\epsilon_0}{t_{ox}}$ and $C_{1D} = \frac{2\epsilon\epsilon_0 L}{\cosh^{-1}[(r + t_{ox})/r]}$ (ref. ⁶²), where ϵ is the dielectric constant of SiO_2 , ϵ_0 is the vacuum permittivity, t_{ox} is the thickness of SiO_2 and r is the radius of the $\text{SnS}_2/\text{WSe}_2$ vdW superlattice roll-ups. The carrier concentration of the $\text{SnS}_2/\text{WSe}_2$ heterobilayer and the $\text{SnS}_2/\text{WSe}_2$ vdW superlattice roll-ups was calculated as $n = C \times (V_g - V_t)$, where V_g is the gate voltage and V_t is the threshold voltage.

Data availability

The data that support the plots within this paper and other findings of this study are available from the corresponding authors upon reasonable request.

51. Zhu, J. T. et al. One-pot selective epitaxial growth of large WS_2/MoS_2 lateral and vertical heterostructures. *J. Am. Chem. Soc.* **142**, 16276–16284 (2020).

52. Liu, H. et al. Growth of large-area homogeneous monolayer transition-metal disulfides via a molten liquid intermediate process. *ACS Appl. Mater. Interfaces* **12**, 13174–13181 (2020).
53. Zhang, C. X. et al. Systematic study of electronic structure and band alignment of monolayer transition metal dichalcogenides in Van der Waals heterostructures. *2D Mater.* **4**, 015026 (2017).
54. Heyd, J., Scuseria, G. E. & Ernzerhof, M. Hybrid functionals based on a screened Coulomb potential. *J. Chem. Phys.* **118**, 8207–8215 (2003).
55. Gianozzi, P. et al. QUANTUM ESPRESSO: a modular and open-source software project for quantum simulations of materials. *J. Phys. Condens. Matter* **21**, 395502 (2009).
56. Schlipf, M. & Gygi, F. Optimization algorithm for the generation of ONCV pseudopotentials. *Comput. Phys. Commun.* **196**, 36–44 (2015).
57. Perdew, J. P., Burke, K. & Ernzerhof, M. Generalized gradient approximation made simple. *Phys. Rev. Lett.* **77**, 3865–3868 (1996).
58. Grimme, S. Semiempirical GGA-type density functional constructed with a long-range dispersion correction. *J. Comput. Chem.* **27**, 1787–1799 (2006).
59. Marini, A., Hogan, C., Grüning, M. & Varsano, D. yambo: an *ab initio* tool for excited state calculations. *Comput. Phys. Commun.* **180**, 1392–1403 (2009).
60. Ismail-Beigi, S. Truncation of periodic image interactions for confined systems. *Phys. Rev. B* **73**, 233103 (2006).
61. Giacomini, R. & Martino, J. A. Modeling silicon on insulator MOS transistors with nonrectangular-gate layouts. *J. Electrochem. Soc.* **153**, G218 (2006).
62. Ford, A. C. et al. Diameter-dependent electron mobility of InAs nanowires. *Nano Lett.* **9**, 360–365 (2009).

Acknowledgements Xidong Duan acknowledges support from the National Key R&D Program of the Ministry of Science and Technology of China (number 2018YFA0703704), the National Natural Science Foundation of China (numbers 51872086, 51991343) and the Hunan Key Laboratory of Two-Dimensional Materials (grant number 2018TP1010) for the work conducted at Hunan University. Y.Z. acknowledges support by the National Natural Science Foundation of China (numbers 51991340, 51991342). The cross-sectional STEM experiments were partly conducted using the facilities of the Irvine Materials Research Institute (IMRI) at the University of California Irvine. I.S. and Z.A. thank the Deanship of Scientific Research at King Saud University for funding of this research through grant PEJP-17-01.

Author contributions B.Z., D.S. and Bailing Li synthesized the vdW heterostructures and developed the rolling-up process to produce vdW superlattices. B.Z., Z.W., Q.Q. and Y.L. performed device fabrication and electrical characterizations. X. Yang, Zucheng Zhang, R. Wu, J.L., H.M., I.S., Z.A. and Y.H. contributed to device fabrication or analysis. J.X., C.G. and Y.P. conducted the theoretical calculations and wrote the related discussions. Z.L., Xingyu Yan, X.P., X.C., F.W., Y.Q. and Y.Z. contributed to the cross-sectional STEM characterizations. Zhengwei Zhang and Bo Li participated in the TEM analysis. B.Z., Z.W., Xidong Duan and Xiangfeng Duan co-wrote the manuscript with input from all of the authors. All authors discussed the results and commented on the manuscript.

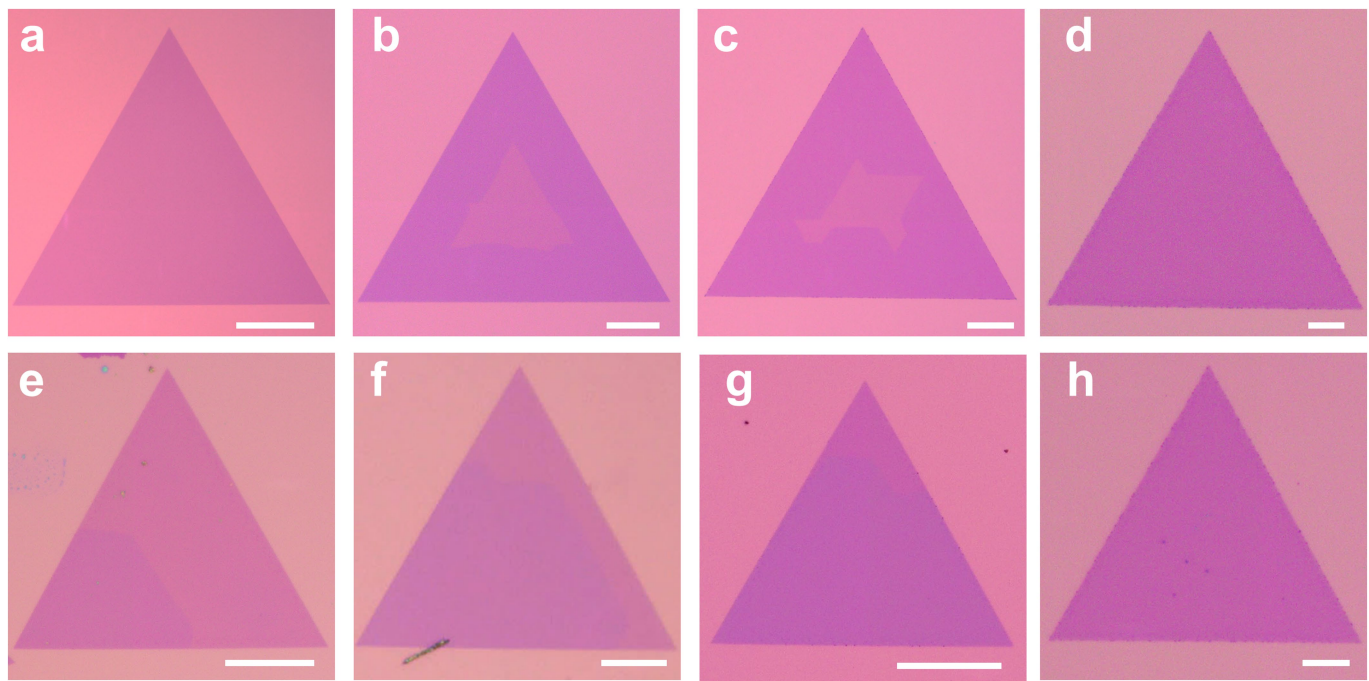
Competing interests The authors declare no competing interests.

Additional information

Correspondence and requests for materials should be addressed to Xidong Duan or Xiangfeng Duan.

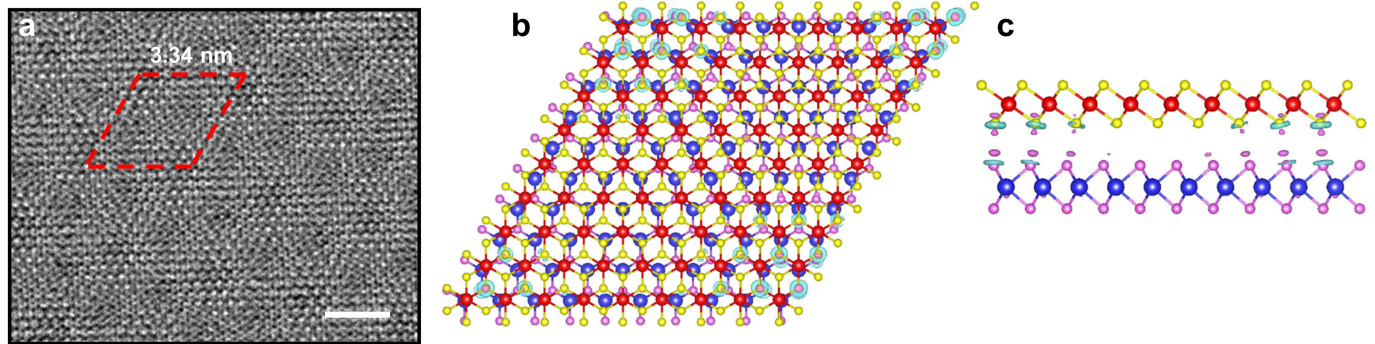
Peer review information *Nature* thanks Hui-Ming Cheng, Jeehwan Kim and Mauricio Terrones for their contribution to the peer review of this work.

Reprints and permissions information is available at <http://www.nature.com/reprints>.

**Extended Data Fig. 1 | Growth of SnS₂/WSe₂ vdW heterostructures.**

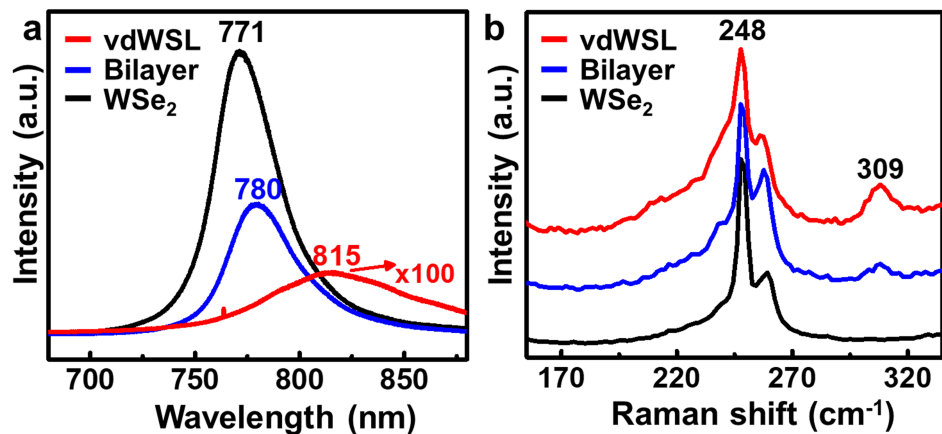
a, Pre-grown WSe₂ monolayer. **b–h**, The top-layer SnS₂ nucleates and grows at the edge (**b–d**) or the corner (**e–h**) of the pre-grown WSe₂ monolayer and

expands laterally to eventually achieve full coverage of monolayer SnS₂ on monolayer WSe₂ (**d, h**). Scale bars, 20 μm.



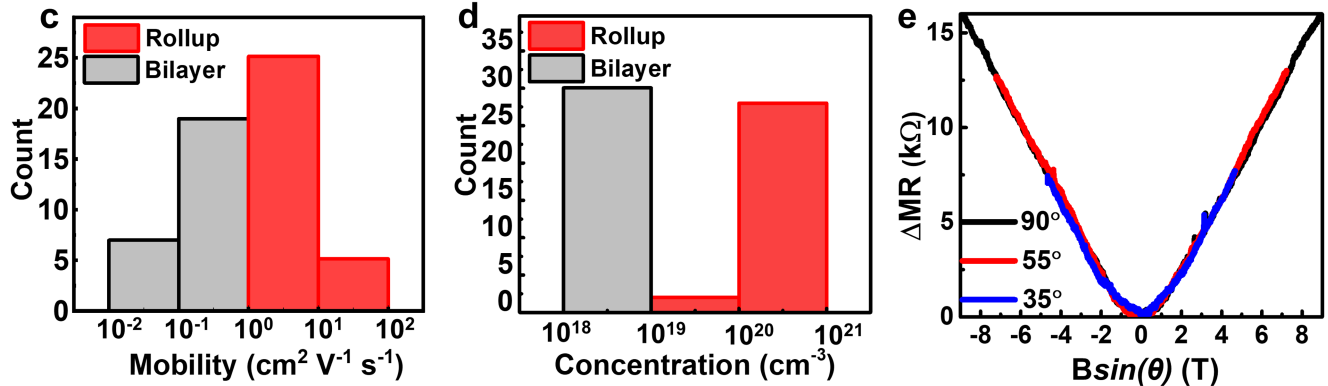
Extended Data Fig. 2 | Atomic structure and differential charge density calculated for the $\text{SnS}_2/\text{WSe}_2$ heterobilayer. **a**, TEM image of the $\text{SnS}_2/\text{WSe}_2$ heterobilayer. The moiré pattern shows a lattice constant of 3.34 nm, and the lattice consists of $10 \times 10 \text{ WSe}_2$ and $9 \times 9 \text{ SnS}_2$. Scale bar, 2 nm. **b, c**, Top (**b**) and side (**c**) view of the atomic structure and the differential charge density

calculated for the $\text{SnS}_2/\text{WSe}_2$ heterobilayer. The amaranth and blue isosurfaces represent negative and positive charge density difference, respectively, between the bilayer vdW heterostructure and the separated layers. The isosurface value is chosen as 0.0005 e au^{-3} .

**Extended Data Fig. 3 | Optical spectra of the SnS₂/WSe₂ systems.**

a, Photoluminescence spectra of a typical WSe₂ monolayer (black line), a SnS₂/WSe₂ heterobilayer (blue line) and a SnS₂/WSe₂ vdW superlattice (red line).

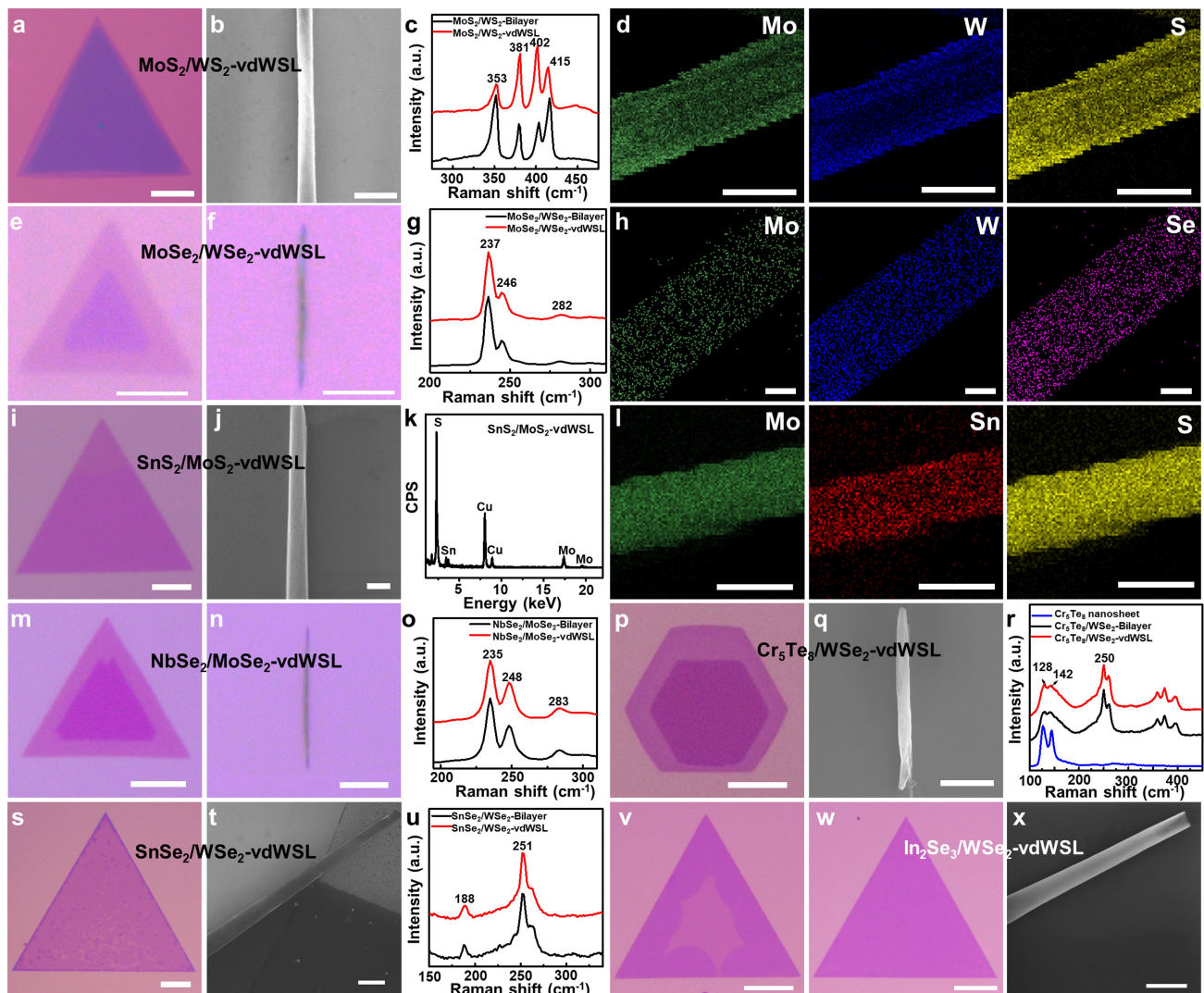
b, Raman spectra of a typical WSe₂ monolayer (black line), SnS₂/WSe₂ heterobilayers (blue line) and a SnS₂/WSe₂ vdW superlattice (red line).



Extended Data Fig. 4 | Schematic illustration and electrical characterizations of SnS₂/WSe₂ roll-up FETs. **a**, SnS₂/WSe₂ heterobilayer FET. **b**, SnS₂/WSe₂ roll-up FET. The pink colour represents WSe₂, yellow denotes SnS₂ and gold represents the Cr/Au contact pads. **c, d**, Statistical distribution of

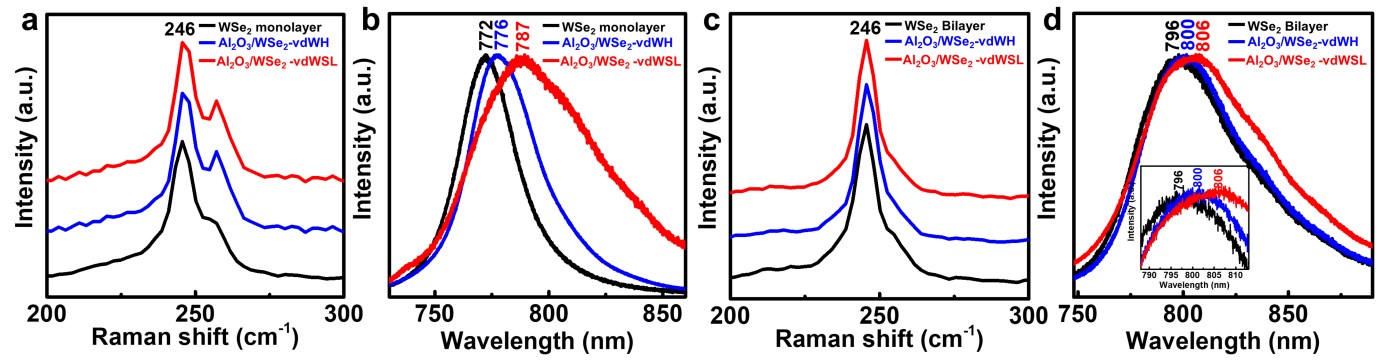
mobility (c) and carrier concentration (d) of SnS₂/WSe₂ heterobilayer FETs and SnS₂/WSe₂ roll-up FETs. **e**, Normalized magnetoresistance of the roll-up vdW superlattices with different rotation angles θ at $T = 3\text{ K}$. Both the shapes and amplitudes overlap when the field is normalized to $B\sin\theta$.

Article



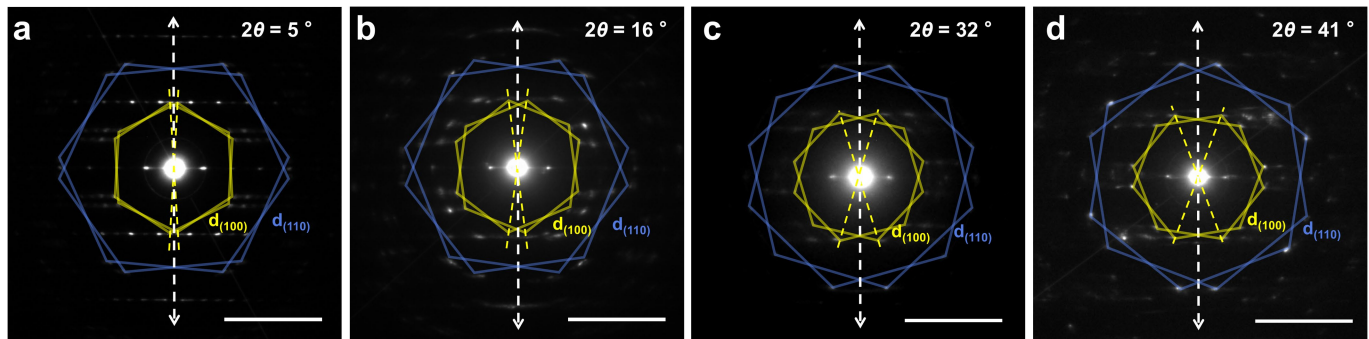
Extended Data Fig. 5 | Various 2D/2D roll-up vdW superlattices. **a**, Optical microscopy image of MoS₂/WS₂ heterobilayer. Scale bar, 10 μm. **b**, SEM image of MoS₂/WS₂ roll-up vdW superlattice. Scale bar, 1 μm. **c**, Raman spectra of a typical MoS₂/WS₂ heterobilayer (black line) and a MoS₂/WS₂ roll-up vdW superlattice (red line). The peaks at 353 cm⁻¹ and 381 cm⁻¹ correspond to the E_{2g}¹ mode of WS₂ and MoS₂, and the peaks at 415 cm⁻¹ and 402 cm⁻¹ correspond to the A_{1g} mode of WS₂ and MoS₂, respectively. **d**, EDS mapping images of Mo, W and S for the MoS₂/WS₂ roll-up vdW superlattice. Scale bars, 200 nm. **e**, **f**, Optical microscopy image of MoSe₂/WSe₂ heterobilayer (**e**) and MoSe₂/WSe₂ roll-up vdW superlattice (**f**). Scale bars, 5 μm. **g**, Raman spectra of a typical MoSe₂/WSe₂ heterobilayer (black line) and a MoSe₂/WSe₂ roll-up vdW superlattice (red line). The peaks at 246 cm⁻¹ and 282 cm⁻¹ correspond to the E_{2g}¹ mode of WSe₂ and MoSe₂, respectively, and the peak at 237 cm⁻¹ to the A_{1g} mode of MoSe₂. **h**, EDS mapping images of Mo, W and Se for the MoSe₂/WSe₂ roll-up vdW superlattice. Scale bars, 100 nm. **i**, Optical microscopy image of the SnS₂/MoS₂ heterobilayer. Scale bar, 5 μm. **j**, SEM image of the SnS₂/MoS₂ roll-up vdW superlattice. Scale bar, 200 nm. **k**, EDS elemental analysis of the SnS₂/MoS₂ roll-up vdW superlattice. **l**, EDS mapping images of Mo, Sn and S for the SnS₂/MoS₂ roll-up vdW superlattice. Scale bars, 200 nm. **m**, **n**, Optical microscopy

image of the NbSe₂/MoSe₂ vdW heterostructure (**m**) and the NbSe₂/MoSe₂ roll-up vdW superlattice (**n**). Scale bars, 5 μm. **o**, Raman spectra of the NbSe₂/MoSe₂ vdW heterostructure (black line) and the NbSe₂/MoSe₂ roll-up vdW superlattice (red line), showing resonance peaks at 235 cm⁻¹ and 283 cm⁻¹, corresponding to the A_{1g} and E_{2g}¹ modes of MoSe₂, respectively, and at 248 cm⁻¹, corresponding to the E_{2g}¹ mode of NbSe₂. **p**, Optical microscopy image of the Cr₅Te₈/WSe₂ vdW heterostructure. Scale bar, 10 μm. **q**, SEM image of the Cr₅Te₈/WSe₂ roll-up vdW superlattice. Scale bar, 1 μm. **r**, Raman spectroscopy of the Cr₅Te₈ nanosheet (blue line), Cr₅Te₈/WSe₂ vdW heterostructure (black line) and Cr₅Te₈/WSe₂ roll-up vdW superlattices (red line). The two characteristic peaks at 128 cm⁻¹ and 142 cm⁻¹ correspond to Cr₅Te₈, and the characteristic peak at 250 cm⁻¹ corresponds to WSe₂. **s**, Optical microscopy image of the SnSe₂/WSe₂ heterobilayer. Scale bar, 20 μm. **t**, SEM image of the SnSe₂/WSe₂ roll-up vdW superlattice. Scale bar, 1 μm. **u**, Raman spectra of the SnSe₂/WSe₂ heterobilayers (black line) and SnSe₂/WSe₂ roll-up vdW superlattice (red line), showing a resonance peak at 188 cm⁻¹, corresponding to the A_{1g} mode of SnSe₂, and at 251 cm⁻¹, corresponding to the E_{2g}¹ mode of WSe₂. **v**, **w**, Optical microscopy images of the In₂Se₃/WSe₂ heterobilayer. Scale bars, 10 μm. **x**, SEM image of a typical In₂Se₃/WSe₂ roll-up vdW superlattice. Scale bar, 1 μm.



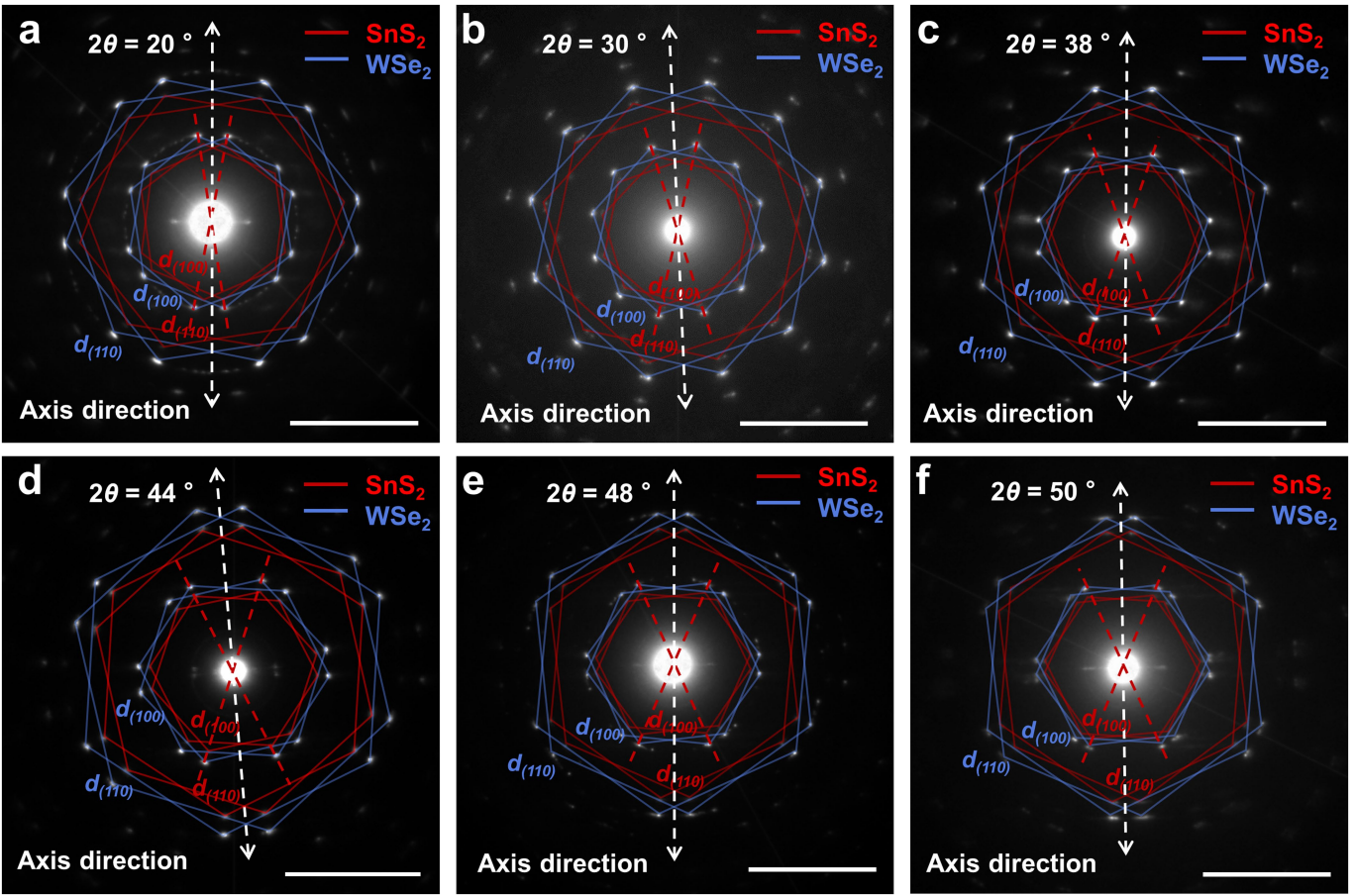
Extended Data Fig. 6 | Optical spectra of $\text{Al}_2\text{O}_3/\text{WSe}_2$ systems. **a, b**, Raman (a) and photoluminescence (b) spectra of monolayer (1L) WSe_2 (black line), $\text{Al}_2\text{O}_3/1\text{L } \text{WSe}_2$ (blue line) heterostructure and $\text{Al}_2\text{O}_3/1\text{L } \text{WSe}_2$ vdW superlattice

(red line). **c, d**, Raman (c) and photoluminescence (d) spectra of bilayer (2L) WSe_2 (black line), $\text{Al}_2\text{O}_3/2\text{L } \text{WSe}_2$ (blue line) heterostructure and $\text{Al}_2\text{O}_3/2\text{L } \text{WSe}_2$ vdW superlattice (red line).



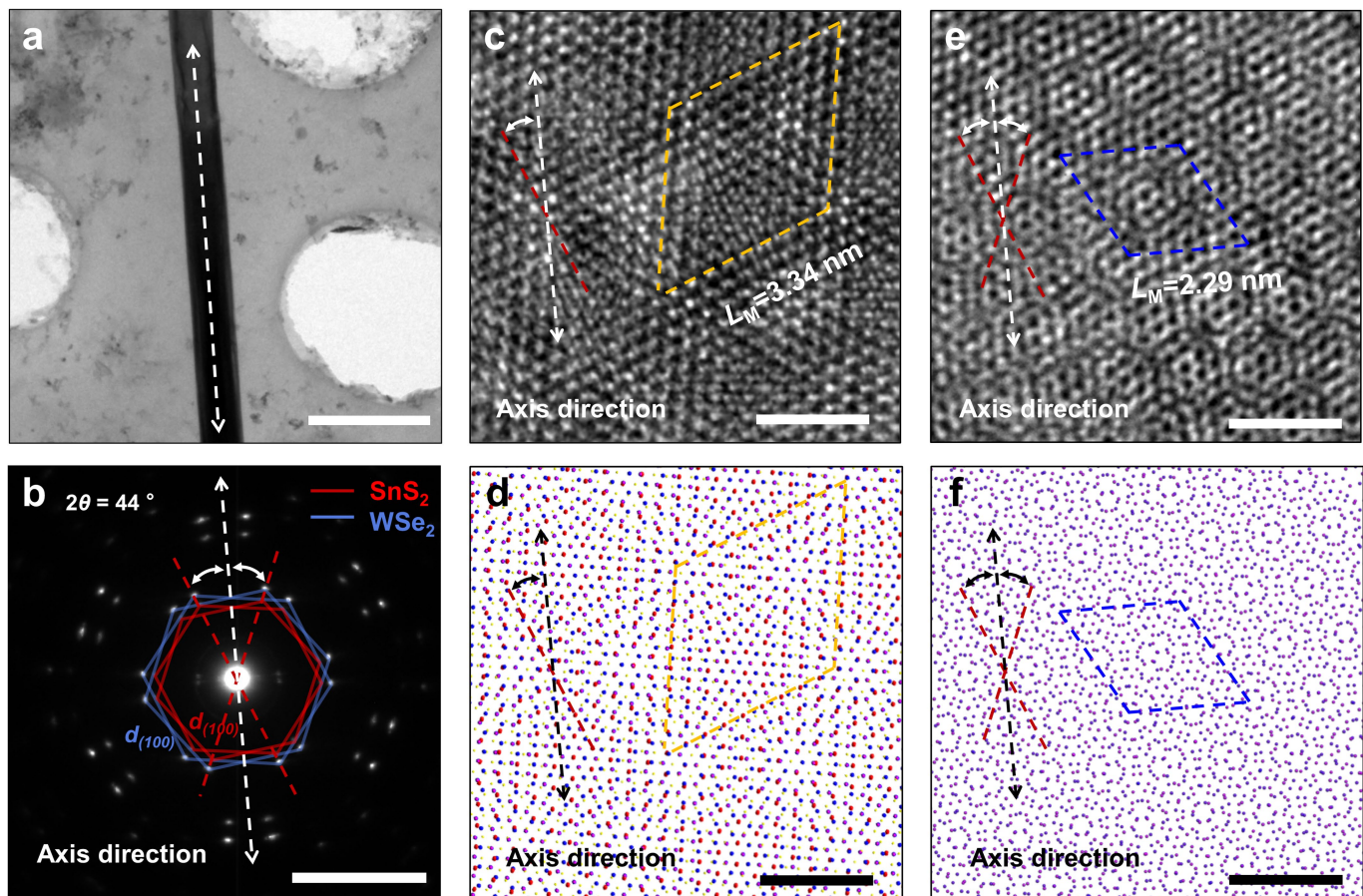
Extended Data Fig. 7 | Selected-area electron diffraction (SAED) images of WSe₂ roll-ups with different chiral angles. The measured distance between spots confirms that the lattice constant of WSe₂ is 0.33 nm. The SAED patterns for different WSe₂ roll-ups show distinct features, with two sets of hexagonal

patterns with a rotation angle of 2θ , where θ is the chiral angle of the roll-up. The chiral angles of the four roll-ups are determined to be $\theta=2.5^\circ$ (a), $\theta=8^\circ$ (b), $\theta=16^\circ$ (c) and $\theta=20.5^\circ$ (d). Scale bars, 5 nm⁻¹.



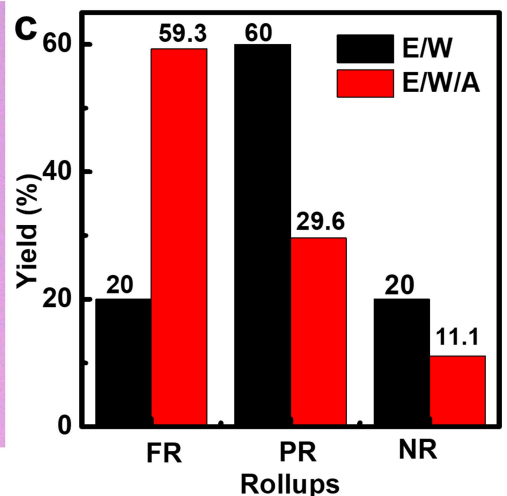
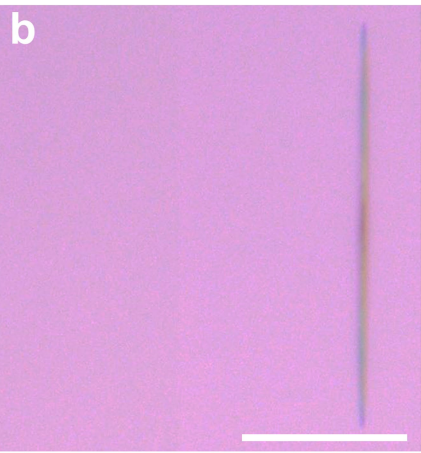
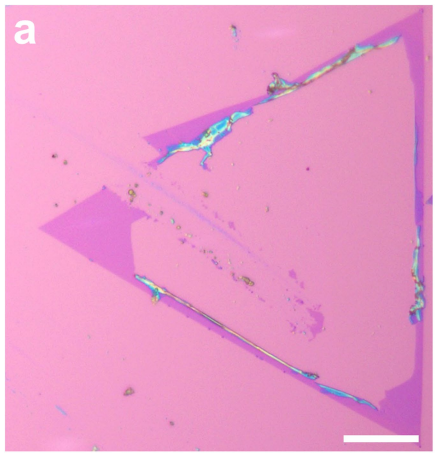
Extended Data Fig. 8 | SAED images of SnS₂/WSe₂ vdW superlattice roll-ups with different chiral angles. The SAED patterns for different SnS₂/WSe₂ roll-ups clearly show the SnS₂ diffraction pattern (red) and the WSe₂ diffraction pattern (blue). The distance measured between spots further confirms that the

lattice constant of WSe₂ is 0.33 nm and that of SnS₂ is 0.37 nm. The diffraction spots of SnS₂ and WSe₂ are well aligned, suggesting epitaxial growth of the heterostructure. The chiral angles are measured to be $\theta=10^\circ$ (a), $\theta=15^\circ$ (b), $\theta=19^\circ$ (c), $\theta=22^\circ$ (d), $\theta=24^\circ$ (e) and $\theta=25^\circ$ (f). Scale bars, 5 nm⁻¹.



Extended Data Fig. 9 | Moiré patterns of SnS₂/WSe₂ roll-up vdW superlattice. **a**, Low-resolution TEM image of a SnS₂/WSe₂ roll-up. Scale bar, 1 μm. **b**, SAED image of the SnS₂/WSe₂ roll-up. Scale bar, 5 nm⁻¹. The white dashed double arrow indicates the axis direction of the roll-up, and the two red dashed lines indicate the major axis of the top wall and bottom wall, which forms a chiral angle of $\theta = \pm 22^\circ$ with the roll-up axis. **c**, High-angle annular dark-field STEM image of the periodic moiré superlattices of the SnS₂/WSe₂ vdW superlattice roll-up; the yellow dashed rhombus is the corresponding moiré unit cells with moiré superlattice constant $L_M = 3.34 \text{ nm}$. Scale bar, 2 nm. The moiré superlattice results from the SnS₂/WSe₂ heterobilayer on the top wall of the roll-up. The red dashed line indicates a major axis of the top-wall SnS₂/WSe₂ heterobilayer and has a chiral angle of $\theta = 22^\circ$ from the roll-up axis

(white dashed double arrow). **d**, The corresponding atomic model of the heterobilayer moiré superlattices of SnS₂/WSe₂. Scale bar, 2 nm. Lattice constants of 0.33 nm and 0.37 nm were used for WSe₂ and SnS₂, respectively. **e**, TEM image of the periodic moiré superlattices of the SnS₂/WSe₂ roll-up. The blue dashed rhombus is the corresponding moiré unit cell with $L_M = 2.29 \text{ nm}$. Scale bar, 2 nm. The moiré superlattice mainly results from WSe₂ in the top wall and the WSe₂ bottom wall, with a folding (twist) angle of 44° between the top and bottom WSe₂. The two red dashed lines indicate the major axes of the top and bottom walls, which form a chiral angle of $\pm 22^\circ$ with the roll-up axis (white dashed double arrow). **f**, The corresponding atomic model of the moiré superlattices of WSe₂/WSe₂ homostructure with a folding angle of 44°. Scale bar, 2 nm.



Extended Data Fig. 10 | The capillary-force-driven rolling-up process used to produce roll-up vdW superlattices. a, b, Optical microscopy images of SnS₂/WSe₂ roll-up obtained with ethanol–water (E/W) (a) and ethanol–water–

ammonia (E/W/A) (b) solutions. Scale bars, 20 μm . c, Statistical distribution of the yield of roll-ups. FR, full roll-ups (for example, b); PR, partial roll-ups (for example, a); NR, no roll-ups.